



Dissipative and dispersive cavity optomechanics with a frequency-dependent mirror






Downloaded from: <https://research.chalmers.se>, 2025-12-06 04:12 UTC

Citation for the original published paper (version of record):

Monsel, J., Ciers, A., Kini Manjeshwar, S. et al (2024). Dissipative and dispersive cavity optomechanics with a frequency-dependent mirror. *Physical Review A*, 109(4).
<http://dx.doi.org/10.1103/PhysRevA.109.043532>

N.B. When citing this work, cite the original published paper.

Dissipative and dispersive cavity optomechanics with a frequency-dependent mirror

Juliette Monsel , Anastasiia Ciers , Sushanth Kini Manjeshwar , Witlef Wieczorek , and Janine Splettstoesser 

Department of Microtechnology and Nanoscience (MC2), Chalmers University of Technology, S-412 96 Göteborg, Sweden



(Received 4 December 2023; accepted 4 April 2024; published 29 April 2024)

An optomechanical microcavity can considerably enhance the interaction between light and mechanical motion by confining light to a subwavelength volume. However, this comes at the cost of an increased optical loss rate. Therefore, microcavity-based optomechanical systems are placed in the unresolved-sideband regime, preventing sideband-based ground-state cooling. A pathway to reduce optical loss in such systems is to engineer the cavity mirrors, i.e., the optical modes that interact with the mechanical resonator. In our work, we analyze such an optomechanical system, whereby one of the mirrors is strongly frequency dependent, i.e., a suspended Fano mirror. This optomechanical system consists of two optical modes that couple to the motion of the suspended Fano mirror. We formulate a quantum-coupled-mode description that includes both the standard dispersive optomechanical coupling as well as dissipative coupling. We solve the Langevin equations of the system dynamics in the linear regime showing that ground-state cooling from room temperature can be achieved even if the cavity is *per se* not in the resolved-sideband regime, but achieves effective sideband resolution through strong-optical-mode coupling. Importantly, we find that the cavity output spectrum needs to be properly analyzed with respect to the effective laser detuning to infer the phonon occupation of the mechanical resonator. Our work also predicts how to reach the regime of nonlinear quantum optomechanics in a Fano-based microcavity by engineering the properties of the Fano mirror.

DOI: [10.1103/PhysRevA.109.043532](https://doi.org/10.1103/PhysRevA.109.043532)

I. INTRODUCTION

Cavity optomechanical systems [1] find applications in quantum technologies [2] and in the exploration of foundational questions [3]. A pertinent regime in cavity optomechanics is sideband resolution, which enables manipulating quantum states of mechanical motion, for example, realizing ground-state cooling of mechanical modes [4,5], optomechanical state swapping [6], or nonclassical mechanical state generation [7–9]. Sideband resolution has been achieved in a variety of optomechanical systems, such as Fabry-Pérot based cavities [10], microtoroids [11], or optomechanical crystals [4]. Commonly, these setups exploit the coupling of a single optical mode to a mechanical resonator.

A major challenge in the field is to combine sideband resolution with large optomechanical coupling on the single-photon level [12,13], where state-of-the-art systems fall two orders of magnitude short to this regime [4,14]. Recently, the concept of strongly frequency-dependent mirrors was introduced in cavity optomechanics [15,16]. It was shown theoretically that frequency-dependent mirrors can reduce the optical linewidth and thereby enable ground-state cooling [16,17] or even strong optomechanical coupling [18]. Such frequency-dependent mirrors rely on Fano resonances [19,20]

and are therefore also referred to as Fano mirrors. Examples of such frequency-dependent mirrors supporting Fano resonances are suspended photonic crystal slabs [15,19,21] or atomic arrays [22–24]. In a common theoretical description of optomechanics with a Fano mirror, two coupled optical modes [20] interact with a mechanical resonator [16,25]. The description of this interaction requires extension of the canonical optomechanical approach [1,16] and enables new capabilities for optomechanical control. Cavity optomechanics exploiting the multimode nature of the optical cavity field has been analyzed in the context of back-action evasion [26], enhancement of nonlinearities [27,28], and when considering the special case of two coupled optical modes that each couple to a mechanical resonator for membrane-in-the-middle systems with realizations in Fabry-Pérot-based cavities [29], optomechanical crystals [28,30], or microtoroids [31]. Our work focuses on a Fano-mirror optomechanical systems, where a comprehensive model and analysis of such optically and optomechanically coupled system is until now missing, thereby blocking the exploitation of opportunities that this type of system offers.

In our work, we provide an extensive analysis of a suspended frequency-dependent mirror coupled to an optical cavity. We consider *both* dispersive as well as dissipative optomechanical couplings [32], which are both observed in experiments with optomechanical microcavities [25]. We find that the two optical modes, i.e., the Fano mode and cavity mode, can strongly couple and will, as a result of this coupling, have a vast impact on the effective cavity decay and the optomechanical coupling. Properly choosing the parameters of this system allows access to various optomechanical

Published by the American Physical Society under the terms of the Creative Commons Attribution 4.0 International license. Further distribution of this work must maintain attribution to the author(s) and the published article's title, journal citation, and DOI. Funded by Bibsam.

regimes, including sideband resolution, single-photon strong coupling, or even ultrastrong coupling, even though the optically *uncoupled* system (namely, in the absence of a Fano mirror) would not be able to reach these regimes. Further, the cavity output spectrum is intricate and needs careful analysis to infer the phonon occupation of the mechanical resonator. Our work extends the theory of Ref. [16], which considers dispersive optomechanics with a Fano mirror focusing on a specific detuning regime only, and of Ref. [33], which considers dispersive and two kinds of dissipative optomechanical couplings but does not address the analysis of a coupled-mirror mode. The advantage of the presented model is that it is versatile and includes all possible mentioned couplings. It hence allows us to express the effect of the Fano mirror in terms of effective parameters in analogy to a standard optomechanical cavity system and to identify parameter regimes where ground-state cooling becomes possible thanks to the Fano-mirror coupling. We also access the intricate connection between the optical readout and the mechanical properties. As required, our general model can be reduced to a specifically chosen simpler experimental setup by simply setting irrelevant couplings to zero. It, thus, also allows comparison to the previously studied systems [16,33].

The paper is structured as follows. We start with a detailed discussion of the model and its dynamics, starting from the purely optical (Sec. II A) and then going to the full optomechanical model (Sec. II B). In Sec. III, we analyze the optomechanical properties of the system and illustrate them with three sets of parameters. Then, in Sec. IV, we apply the insights we have gained on the system to back-action cooling, evidencing that a suitable engineering of the Fano mirror allows for ground-state cooling at room temperature. Finally, Sec. V details how the quantum nonlinear regime could be reached with a microcavity-based optomechanical device. We conclude in Sec. VI. The Appendix provides all necessary theoretical details of the approach that were left out in the main part of the paper for improved readability.

II. QUANTUM COUPLED-MODE MODEL

In this section, we introduce the model Hamiltonians and analyze the dynamics of an optomechanical system with a Fano mirror. We start with the purely optical part of this coupled-mode system (Fano-mirror mode coupled to cavity mode) and then introduce the mechanical mode and its coupling to the optics. Compared to a previous analysis [16], we add the dissipative optomechanical contributions [33,34] to the coupled-mode model of a cavity with one Fano mirror and the optomechanical modulation of the properties of the Fano mirror.

A. Optical cavity with Fano mirror

1. Optical-modes model

We study a double-sided optical cavity, as depicted in Fig. 1, but disregard the mechanical degree of freedom at this initial stage. The cavity consists of a strongly frequency-dependent mirror (Fano mirror), such as a photonic crystal slab on the left and a standard, highly reflective mirror on the right, inspired by Refs. [15,25,35]. We consider a single opti-

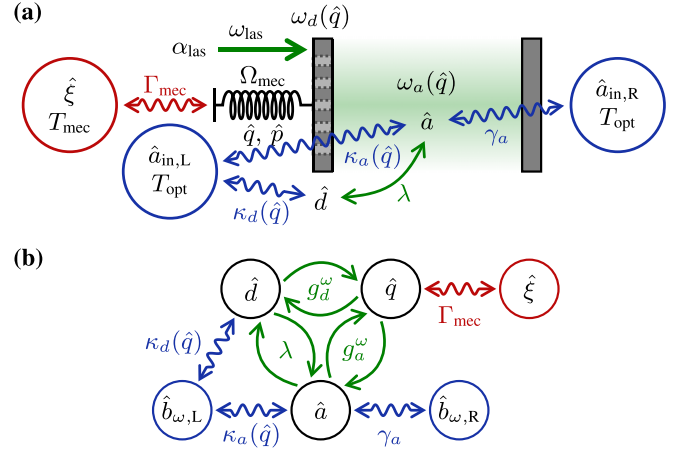


FIG. 1. (a) Sketch of the optomechanical setup, consisting of a double-sided optical cavity with one movable frequency-dependent mirror, and (b) the setup's coupled-mode picture. The cavity mode (\hat{a}) is coupled to electromagnetic environments on each side of the double-sided cavity (blue circles). The left mirror is frequency dependent and its internal mode (\hat{d}) is also coupled to the left electromagnetic environment. The left mirror has a mechanical degree of freedom (\hat{q}), which is coupled to a phonon environment (red circle). The cavity is driven with a laser at frequency ω_{las} . See Secs. II A 1 and II B 1 for definitions of all indicated variables.

cal cavity mode of frequency ω_a , associated with the photon annihilation operator \hat{a} . In addition, the frequency dependence of the Fano mirror is modeled with another harmonic mode of frequency ω_d and photon annihilation operator \hat{d} . Due to the overlap between this guided mirror mode and the cavity mode, these two optical modes are coupled and they are described by the Hamiltonian [16]

$$\hat{H}_{\text{opt}} = \hbar\omega_a\hat{a}^\dagger\hat{a} + \hbar\omega_d\hat{d}^\dagger\hat{d} + \hbar\lambda(\hat{a}^\dagger\hat{d} + \hat{d}^\dagger\hat{a}), \quad (1)$$

considering here the case of an even Fano mode.¹ The coupling strength λ can be engineered via the photonic crystal or via the evanescent coupling of the two modes a and d . The cavity mode is also coupled to the electromagnetic environments on both sides of the cavity, giving rise to the respective loss rates κ_a and γ_a , while the mirror mode is only coupled to the left-hand-side environment, giving rise to the loss rate κ_d .

2. Langevin equations

Here, we first present the Langevin equations [16,36] of the optical system only, driven by a laser at frequency ω_{las} , and obtain, in the frame rotating at the laser frequency,

$$\begin{bmatrix} \dot{\hat{a}} \\ \dot{\hat{d}} \end{bmatrix} = -i \begin{bmatrix} \Delta_a - i(\kappa_a + \gamma_a) & \mathcal{G} \\ \mathcal{G} & \Delta_d - i\kappa_d \end{bmatrix} \begin{bmatrix} \hat{a} \\ \hat{d} \end{bmatrix} + \text{input fluct.} \quad (2)$$

¹More generally, this coupling is of the form $\hbar\lambda(\hat{a} + \hat{a}^\dagger)(\hat{d} + \hat{d}^\dagger)$. But, depending on the symmetry of the guided mirror mode, the dominant term in the coupling is either the beam-splitter mode considered here (even mirror mode) or the two-mode-squeezing term $\hat{a}\hat{d} + \hat{a}^\dagger\hat{d}^\dagger$ (odd mirror mode) [16]. The analysis conducted in this article could straightforwardly be adapted to an odd mirror mode as well.

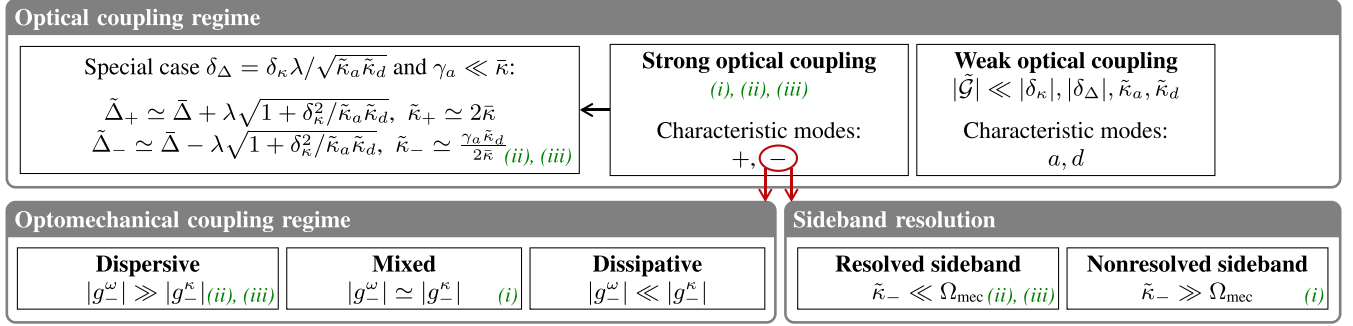


FIG. 2. Illustration of the relevant parameter regimes. Each box details one aspect of the different regimes for a specific set of parameters. We have indicated in green in which regime the studied devices (see Sec. IID and Table I) are operating. In this article, where we focus on strong optical coupling, the effective “−” mode (highlighted in red) has a small linewidth and therefore characterizes the physics of the device, in contrast to the highly damped (and hence irrelevant) “+” mode. The optomechanical-coupling and sideband-resolution regimes in the lower two boxes therefore refer to the “−” mode.

We have introduced the total optical coupling strength $\mathcal{G} = \lambda - i\sqrt{\kappa_a \kappa_d}$, including a contribution arising from the dissipative coupling of the two modes to the same environment [16], as well as the detunings $\Delta_c = \omega_c - \omega_{\text{las}}$, with $c = a, d$. From the matrix characterizing the mode coupling, we obtain the complex eigenvalues

$$\Omega_\pm = \tilde{\Delta} - i\tilde{\kappa} \pm \sqrt{(\delta_\Delta - i\delta_\kappa)^2 + \mathcal{G}^2}, \quad (3)$$

which correspond to the effective resonance frequencies $\Delta_\pm = \text{Re}(\Omega_\pm)$, namely, the real part of Ω_\pm , and their effective loss rates $\kappa_\pm = -\text{Im}(\Omega_\pm)$, namely, the imaginary part of Ω_\pm . We have defined the average detuning $\tilde{\Delta} = (\Delta_a + \Delta_d)/2$ and the average loss rate $\tilde{\kappa} = (\kappa_a + \gamma_a + \kappa_d)/2$, as well as the difference in detunings $\delta_\Delta = (\Delta_a - \Delta_d)/2$ and the difference in loss rates $\delta_\kappa = (\kappa_a + \gamma_a - \kappa_d)/2$.

From the expression of the eigenvalues, Eq. (3), we see that we get the expected weak-coupling result for small \mathcal{G} (small compared to the difference in frequency and loss rate between the optical modes a and d). However, this weak-coupling regime is not relevant here since the dissipative part of \mathcal{G} is $\sqrt{\kappa_a \kappa_d}$ which is close to the order of $\tilde{\kappa}$. Furthermore, in our recent experimental realization employing a Fano mirror [25], it was found that λ is larger than $\tilde{\kappa}$. In that case, the eigenmodes differ significantly from the cavity and mirror modes and it is rather the “−” eigenmode that gives an intuition of the behavior of the experimental system. We will now show that we can use this optical coupling to engineer the effective optical loss rates and, in particular, make κ_- several orders of magnitude smaller than κ_d, κ_a . This is a prospective way to reach the (effective) resolved-sideband regime in an optomechanical system.

The effective modes discussed above are useful to interpret experimental results [25] and to identify relevant parameter regimes (Fig. 2). While the identified eigenvalues Ω_\pm will occur in a number of analytical expressions in the remainder of this paper, it is in general not convenient to use the performed diagonalization in order to fully reformulate the Langevin equations of the full optomechanical system. First, we have not taken into account the optomechanical couplings of interest here during the diagonalization, so the optomechanical part of the equations would not become simpler. Second, while the

operators \hat{c} fulfill standard canonical commutation relations, $[\hat{c}, \hat{c}^\dagger] = 1$, these “+” and “−” modes do not. The reason for this is that the operators corresponding to the eigenmodes are functions of the operators \hat{c} as well as of their detunings and loss rates.

B. Optomechanical setup

1. Full optomechanical model

We now come to the optomechanical model, where the Fano mirror is suspended. It hence also has a mechanical degree of freedom of frequency Ω_{mec} and dimensionless position and momentum quadratures \hat{q} and \hat{p} .

The overall system exhibits optomechanical effects both through dispersive and dissipative couplings, namely, the respective modulations of the optical frequencies $\omega_a(\hat{q})$ and $\omega_d(\hat{q})$, and loss rates $\kappa_a(\hat{q})$ and $\kappa_d(\hat{q})$, by the mechanical motion. The position dependence of $\omega_a(\hat{q})$ comes from the change in the cavity length caused by the mechanical motion. But this change also modifies the reflection and transmission coefficients of the left mirror at the cavity resonance, affecting the loss rate $\kappa_a(\hat{q})$, which therefore also becomes position dependent. For photonic crystals, the mechanical-position dependence of the mirror mode parameters $\omega_d(\hat{q})$ and $\kappa_d(\hat{q})$ comes from the local deformation of the lattice period and air-hole radius due to the mechanical vibrations. Furthermore, in the case of microcavities [25], there can be an additional effect due to evanescent electromagnetic fields making the properties of the Fano mode dependent on the distance to the fixed mirror. For most optomechanics experiments, the dependence of the optical parameters on the mechanical position \hat{q} can be approximated as linear [1], leading to linear optomechanical couplings $\kappa_c(\hat{q}) = \kappa_c + \sqrt{2}g_c^\kappa \hat{q}$ and $\omega_c(\hat{q}) = \omega_c - \sqrt{2}g_c^\omega \hat{q}$. Taking into account both optical modes $c = a, d$ and dispersive g_c^ω as well as dissipative couplings g_c^κ , we define the four single-photon optomechanical couplings

$$g_c^\omega = -\frac{1}{\sqrt{2}} \left(\frac{\partial \omega_c}{\partial \hat{q}} \right)_{q=0}, \quad g_c^\kappa = \frac{1}{\sqrt{2}} \left(\frac{\partial \kappa_c}{\partial \hat{q}} \right)_{q=0}. \quad (4)$$

In the following ω_c and κ_c will always denote the frequencies and loss rates evaluated at zero mechanical displacement. The sign convention we have chosen for the dispersive coupling is

TABLE I. Parameters used for the three studied devices: (i) experimental device from Ref. [25], (ii) device with matching optical modes, $\delta_\Delta = \delta_\kappa = 0$, and (iii) device with $\delta_\Delta = \delta_\kappa \lambda / \sqrt{\tilde{\kappa}_a \tilde{\kappa}_d}$. For devices (ii) and (iii), we have chosen larger state-of-the-art mechanical frequencies and quality factors [39]. The optical loss rates given here are the ones evaluated at the average mechanical displacement \bar{q} ($\tilde{\kappa}_a$, $\tilde{\kappa}_d$) but for all three devices the difference with the parameters evaluated at zero displacement (κ_a , κ_d) is negligible. The laser powers indicated for devices (ii) and (iii) are chosen such that the devices are in the weak-coupling regime to show the blue and red sidebands in Figs. 5 and 7. Laser powers required for achieving ground-state cooling, as discussed in Sec. IV B, are however larger, of the order of 10 W and 10 mW, respectively (see Fig. 8) in Sec. V.

Parameter	Description	Device (i)	Device (ii)	Device (iii)
<i>Optical modes</i>				
$\delta_\Delta/2\pi$	Effective detuning between the cavity and mirror modes (Hz)	-1.42×10^{10}	0	1.97×10^{13}
$\gamma_a/2\pi$	Coupling between the cavity mode and the right environment (Hz)	3.66×10^{11}	1.30×10^5	6.00×10^8
$\tilde{\kappa}_a/2\pi$	Coupling between the cavity mode and the left environment (Hz)	2.12×10^{12}	2.12×10^{12}	1.00×10^{13}
$\tilde{\kappa}_d/2\pi$	Coupling between the mirror mode and the left environment (Hz)	3.80×10^{12}	2.12×10^{12}	1.08×10^9
$\lambda/2\pi$	Coupling between the cavity and mirror modes (Hz)	4.09×10^{12}	4.09×10^{12}	4.09×10^{11}
P_{las}	Laser power used in Figs. 3–7 (μW)	150	50	0.256
<i>Mechanical mode</i>				
$\Omega_{\text{mec}}/2\pi$	Bare mechanical frequency (Hz)	5.14×10^5	1.3×10^6	1.3×10^6
$\Gamma_{\text{mec}}/2\pi$	Bare mechanical damping rate (Hz)	17.1	9.3×10^{-3}	9.3×10^{-3}
Q_{mec}	Mechanical quality factor	3×10^4	1.4×10^8	1.4×10^8
<i>Single-photon optomechanical couplings</i>				
$g_a^\omega/\Omega_{\text{mec}}$	Cavity dispersive optomechanical coupling	1.6	6.5×10^{-5}	6.5×10^{-5}
$g_d^\omega/\Omega_{\text{mec}}$	Mirror dispersive optomechanical coupling	-3.5	-1.4×10^{-4}	-1.4×10^{-4}
$g_a^\kappa/\Omega_{\text{mec}}$	Cavity dissipative optomechanical coupling	1.5	6.0×10^{-5}	6.0×10^{-5}
$g_d^\kappa/\Omega_{\text{mec}}$	Mirror dissipative optomechanical coupling	6.3	2.5×10^{-4}	7.1×10^{-8}
<i>Effective optical “–” mode</i>				
$\tilde{\kappa}_-/ \Omega_{\text{mec}}$	Sideband resolution	5.4×10^5	0.05	0.05
$g_-^\omega/\Omega_{\text{mec}}$	Single-photon dispersive ultrastrong-coupling ratio	-0.97	-3.8×10^{-5}	-1.4×10^{-4}
$g_-^\kappa/\Omega_{\text{mec}}$	Single-photon dissipative ultrastrong-coupling ratio	0.065	2.9×10^{-12}	3.8×10^{-12}
$g_-^\omega/\tilde{\kappa}_-$	Single-photon dispersive strong-coupling ratio	-1.8×10^{-6}	-7.5×10^{-4}	-2.8×10^{-3}
$g_-^\kappa/\tilde{\kappa}_-$	Single-photon dissipative strong-coupling ratio	-1.2×10^{-7}	5.7×10^{-11}	7.7×10^{-11}

such that the coupling strength for a standard Fabry-Pérot cavity mode is positive. The mechanical mode and the dispersive optomechanical effects are then described by the Hamiltonian

$$\hat{H}_{\text{om}} = \frac{\hbar \Omega_{\text{mec}}}{2} (\hat{p}^2 + \hat{q}^2) - \sqrt{2} \sum_{c=a,d} \hbar g_c^\omega \hat{c}^\dagger \hat{c} \hat{q}. \quad (5)$$

The mechanical mode is of course coupled to a phononic environment, giving rise to the damping rate Γ_{mec} . However, in most optomechanical setups, this damping rate is orders of magnitude smaller compared to the other relevant frequencies. So, we will not consider it at the level of the Hamiltonian, but rather on the level of the Langevin equations, discussed in the next subsection. Details about the microscopic modeling of such an environment can be found, for instance, in Ref. [37]. Then, the whole setup is described by the total Hamiltonian $\hat{H}_{\text{tot}} = \hat{H}_{\text{om}} + \hat{H}_{\text{opt}} + \hat{H}_{\text{env}} + \hat{H}_{\text{int}}$ [16,34], with the optical environment Hamiltonian $\hat{H}_{\text{env}} = \sum_{\mu=L,R} \int d\omega \hbar \omega \hat{b}_{\omega,\mu}^\dagger \hat{b}_{\omega,\mu}$ and the interaction Hamiltonian for the coupling between system and optical environments

$$\begin{aligned} \hat{H}_{\text{int}} = & \sum_c i\hbar \left[\sqrt{\frac{\kappa_c}{\pi}} + \frac{g_c^\kappa}{\sqrt{2\pi\kappa_c}} \hat{q} \right] \int d\omega (\hat{c}^\dagger \hat{b}_{\omega,L} - \hat{b}_{\omega,L}^\dagger \hat{c}) \\ & + i\hbar \sqrt{\frac{\gamma_a}{\pi}} \int d\omega (\hat{a}^\dagger \hat{b}_{\omega,R} - \hat{b}_{\omega,R}^\dagger \hat{a}). \end{aligned} \quad (6)$$

The photon annihilation operators $\hat{b}_{\omega,\mu}$, with $\mu = L, R$, relate to the mode of frequency ω in the corresponding environment. We do not explicitly include the laser drive of frequency ω_{las} depicted in Fig. 1(a) in the Hamiltonian \hat{H}_{tot} because we model it as a part of the left environment, namely, taking $\langle \hat{b}_{\omega,L} \rangle \propto \alpha_{\text{las}} \delta(\omega - \omega_{\text{las}})$ (see next subsection). The amplitude of the laser drive α_{las} is related to the laser power by $P_{\text{las}} = \hbar \omega_{\text{las}} |\alpha_{\text{las}}|^2$. The expression (6) of the interaction Hamiltonian \hat{H}_{int} already contains several approximations. First, as commonly done for such systems [16,34,36], we have neglected the two-mode-squeezing terms $\hat{c}^\dagger \hat{b}_{\omega,\mu}^\dagger + \hat{c} \hat{b}_{\omega,\mu}$. Second, we have used the Markov approximation [36], namely, we have assumed that the coupling of *both* modes *a* and *d* is frequency independent. Note, however, that the *effective* dynamics of the cavity mode, when integrating out the Fano mirror mode, is non-Markovian [16]. Indeed, delays and memory effects arise in the reduced evolution of mode *a* due to its interaction with the Fano mirror since $|\mathcal{G}|$ is not negligible compared to κ_a . This will not be our focus, though, and we always consider the joint evolution of the two optical modes in the following, which is Markovian.

We have, until here, expressed all optomechanical couplings in terms of the original modes $c = a, d$. However, coming back to the coupled modes introduced in Sec. II A, insights about the relevant coupling regimes can be gained. The corresponding effective dispersive and dissipative

optomechanical couplings are given by

$$g_{\pm}^{\omega} = -\frac{1}{\sqrt{2}} \left(\frac{\partial \Delta_{\pm}}{\partial \bar{q}} \right)_{\bar{q}=0}, \quad g_{\pm}^{\kappa} = \frac{1}{\sqrt{2}} \left(\frac{\partial \kappa_{\pm}}{\partial \bar{q}} \right)_{\bar{q}=0}. \quad (7)$$

Interestingly, we can have $\kappa_{-} < \Omega_{\text{mec}}$, even in microcavities where the optical losses are many orders of magnitude larger than the mechanical frequency.

First, in the simple case where the mirror mode and cavity mode have identical characteristics, namely, $\delta_{\Delta} = \delta_{\kappa} = 0$, Eq. (3) becomes $\Omega_{\pm} = \bar{\Delta} \pm \lambda - i\bar{\kappa}(1 \pm \sqrt{1 - \gamma_a/\bar{\kappa}})$. In the limit $\gamma_a \ll \bar{\kappa}$, we then find that $\kappa_{-} \simeq \gamma_a/2$ and therefore the optical linewidth can be significantly reduced, even reaching the resolved sideband limit if² $\gamma_a < 2\Omega_{\text{mec}}$. The corresponding effective dispersive and dissipative couplings then become $g_{-}^{\omega} = (g_a^{\omega} + g_d^{\omega})/2$ and $g_{-}^{\kappa} \simeq \gamma_a(g_d^{\kappa} - g_a^{\kappa})/4\bar{\kappa}$, leading in most cases to a mainly dispersive optomechanical coupling $g_{-}^{\omega} \gg g_{-}^{\kappa}$.

Furthermore, when $\delta_{\Delta} = \delta_{\kappa}\lambda/\sqrt{\kappa_a\kappa_d}$, we can easily compute the real and imaginary parts of Eq. (3), $\Delta_{\pm} = \bar{\Delta} \pm \lambda\sqrt{1 + \delta_{\kappa}^2/\kappa_a\kappa_d}$ and $\kappa_{\pm} = \bar{\kappa} \pm \sqrt{\bar{\kappa}^2 - \gamma_a\kappa_d}$. In this limit and in the regime $\gamma_a \ll \bar{\kappa}$ of interest here, we have $\kappa_{-} \simeq \gamma_a\kappa_d/2\bar{\kappa}$. It is hence useful to study the case where $\kappa_d \ll \kappa_a$ when γ_a cannot be made of the same order of magnitude as Ω_{mec} . A summary of the possible parameter regimes, focusing on the “-” effective mode, is given in Fig. 2.

2. Langevin equations

Following the usual derivation for input-output equations [16,36] (see details in Appendix A 1), we obtain the Langevin equations, in the frame rotating at the laser frequency,

$$\begin{aligned} \dot{\hat{a}} &= -(i\Delta_a + \kappa_a + \gamma_a)\hat{a} + \sqrt{2}(ig_a^{\omega} - g_a^{\kappa})\hat{q}\hat{a} - i\mathcal{G}\hat{d} \\ &\quad - \sqrt{2}g^{\kappa,\text{sym}}\hat{q}\hat{a} + \left(\sqrt{2\kappa_a} + \frac{g_a^{\kappa}}{\sqrt{\kappa_a}}\hat{q}\right)\hat{b}_{\text{in,L}} + \sqrt{2\gamma_a}\hat{b}_{\text{in,R}}, \\ \dot{\hat{d}} &= -(i\Delta_d + \kappa_d)\hat{d} + \sqrt{2}(ig_d^{\omega} - g_d^{\kappa})\hat{q}\hat{d} - i\mathcal{G}\hat{a} \\ &\quad - \sqrt{2}g^{\kappa,\text{sym}}\hat{q}\hat{d} + \left(\sqrt{2\kappa_d} + \frac{g_d^{\kappa}}{\sqrt{\kappa_d}}\hat{q}\right)\hat{b}_{\text{in,L}}, \\ \dot{\hat{q}} &= \Omega_{\text{mec}}\hat{p}, \\ \dot{\hat{p}} &= -\Omega_{\text{mec}}\hat{q} - \Gamma_{\text{mec}}\hat{p} + i\sqrt{2}g^{\kappa,\text{asym}}(\hat{a}^{\dagger}\hat{d} - \hat{d}^{\dagger}\hat{a}) \\ &\quad + \sum_c \left[\sqrt{2}g_c^{\omega}\hat{c}^{\dagger}\hat{c} - i\frac{g_c^{\kappa}}{\sqrt{\kappa_c}}(\hat{c}^{\dagger}\hat{b}_{\text{in,L}} - \hat{b}_{\text{in,L}}^{\dagger}\hat{c}) \right] + \sqrt{\Gamma_{\text{mec}}}\hat{\xi}. \end{aligned} \quad (8)$$

We have denoted the effective optomechanical couplings arising from the dissipative optomechanical effects combined with the coupling of the mirror mode and cavity mode to the

same (left) environment as

$$\begin{aligned} g^{\kappa,\text{sym}} &= \frac{\sqrt{\kappa_a\kappa_d}}{2} \left(\frac{g_a^{\kappa}}{\kappa_a} + \frac{g_d^{\kappa}}{\kappa_d} \right), \\ g^{\kappa,\text{asym}} &= \frac{\sqrt{\kappa_a\kappa_d}}{2} \left(\frac{g_a^{\kappa}}{\kappa_a} - \frac{g_d^{\kappa}}{\kappa_d} \right). \end{aligned} \quad (9)$$

The cavity is driven through the left mirror, therefore, the average input amplitudes, in $\sqrt{\text{Hz}}$, are $\langle \hat{b}_{\text{in,L}} \rangle = \alpha_{\text{las}}$ and $\langle \hat{b}_{\text{in,R}} \rangle = 0$.

The optical output fields of interest are given by the input-output relations [36]

$$\begin{aligned} \hat{b}_{\text{out,L}}(t) &= \hat{b}_{\text{in,L}}(t) - \sum_c \left(\sqrt{2\kappa_c} + \frac{g_c^{\kappa}}{\sqrt{\kappa_c}}\hat{q}(t) \right) \hat{c}(t), \\ \hat{b}_{\text{out,R}}(t) &= \hat{b}_{\text{in,R}}(t) - \sqrt{2\gamma_a}\hat{a}(t). \end{aligned} \quad (10)$$

In the limit $g_a^{\kappa}, g_d^{\omega}, g_d^{\kappa} \rightarrow 0$, with only dispersive optomechanical effects on the cavity mode, Eqs. (10) and (8) give back the results derived in Ref. [16].

C. Linearized dynamics

From now on, we consider that the laser drive is rather strong, such that the numbers of photons in the light fields in the cavity and in the mirror are large compared to their fluctuations. Furthermore, the optical frequencies are such that $\hbar\omega_a, \hbar\omega_d \gg k_B T_{\text{opt}}$, therefore, we can consider that the temperature T_{opt} in optical environments is zero and neglect thermal fluctuations. As a consequence, we can rewrite $\hat{b}_{\text{in,L}} = \alpha_{\text{las}} + \hat{a}_{\text{in,L}}$ and $\hat{b}_{\text{in,R}} = \hat{a}_{\text{in,R}}$, where $\hat{a}_{\text{in},\mu}$ corresponds to the vacuum fluctuations and its only nonzero correlation function is

$$\langle \hat{a}_{\text{in},\mu}(t)\hat{a}_{\text{in},\mu}^{\dagger}(t') \rangle = \delta(t - t'). \quad (11)$$

In contrast, concerning the mechanics, we are in the high-temperature limit $\hbar\Omega_{\text{mec}} \ll k_B T_{\text{mec}}$. The input noise of the mechanics is determined by $\langle \hat{\xi} \rangle = 0$ and by the correlation function³

$$\langle \hat{\xi}(t)\hat{\xi}(t') \rangle = (2\bar{n}_{\text{mec}} + 1)\delta(t - t'), \quad (12)$$

with the average phonon number in the mechanical environment $\bar{n}_{\text{mec}} = [\exp(\hbar\Omega_{\text{mec}}/k_B T_{\text{mec}}) - 1]^{-1}$. We now split all the operators into a semiclassical average value and a fluctuation operator: $\hat{a} = \bar{a} + \delta\hat{a}$, $\hat{d} = \bar{d} + \delta\hat{d}$, $\hat{q} = \bar{q} + \delta\hat{q}$, and $\hat{p} = \bar{p} + \delta\hat{p}$.

1. Semiclassical steady state

As a first step towards the solution of the Langevin equations (8), we here present the semiclassical steady-state

²Note that one does not need to have perfectly identical optical modes to reach this effective resolved-sideband regime. Instead it needs to be in the regime $\bar{\kappa} \lesssim \lambda$, $\gamma_a < 2\Omega_{\text{mec}}$ and $\delta_{\Delta}^2/\bar{\kappa}, \delta_{\kappa}^2/\bar{\kappa} \ll \Omega_{\text{mec}}$.

³For simplicity, we approximate here the correlation function by its classical value, but we checked that this does not impact our results. In general, this approximation might give inconsistencies in the quantum regime, even in the high-temperature limit, because it does not preserve the commutation relations between \hat{q} and \hat{p} [38]. We discussed in particular the impact on the phonon number in the mechanics in the Appendix of a previous work [17].

solution. It is given by the expressions

$$\begin{aligned}\bar{a} &= i \frac{\lambda \sqrt{2\tilde{\kappa}_d} - \tilde{\Delta}_d \sqrt{2\tilde{\kappa}_a}}{\tilde{\Omega}_+ \tilde{\Omega}_-} \alpha_{\text{las}}, \\ \bar{d} &= \frac{i(\lambda \sqrt{2\tilde{\kappa}_a} - \tilde{\Delta}_a \sqrt{2\tilde{\kappa}_d}) - \gamma_a \sqrt{2\tilde{\kappa}_d}}{\tilde{\Omega}_+ \tilde{\Omega}_-} \alpha_{\text{las}}, \\ \bar{q} &= \frac{\sqrt{2}}{\Omega_{\text{mec}}} \sum_c \left[g_c^\omega |\bar{c}|^2 - i \frac{g_c^\kappa}{\sqrt{2\kappa_c}} (\bar{c}^* \alpha_{\text{las}} - \bar{c} \alpha_{\text{las}}^*) \right] \\ &\quad + \frac{i\sqrt{2}}{\Omega_{\text{mec}}} g^{\kappa, \text{asym}} (\bar{a}^* \bar{d} - \bar{d}^* \bar{a}), \\ \bar{p} &= 0.\end{aligned}\quad (13)$$

Here, we have introduced a tilde to indicate that parameters are taken at the average mechanical displacement \bar{q} . We consider the most general situation of different optomechanical couplings. In particular, the detunings are generally impacted by dispersive optomechanical couplings $\tilde{\Delta}_c = \Delta_c - \sqrt{2}g_c^\omega \bar{q}$, while the loss rates $\tilde{\kappa}_c = \kappa_c + \sqrt{2}g_c^\omega \bar{q}$ are impacted by dissipative optomechanical couplings. Also the effective coupling between cavity and Fano mirror $\tilde{\mathcal{G}} = \lambda - i\sqrt{\tilde{\kappa}_a \tilde{\kappa}_d}$ has a contribution due to the dissipative optomechanical couplings. Note, however, that these shifts in the steady-state solution due to the average mechanical displacement \bar{q} are negligibly small in typical experiments considered in the remainder of this paper. This also means that while the system of equations (13) is nonlinear, we assume in the following that we are in a parameter regime where the displacement corrections are small and the system is stable. Equations (13) hence give a single well-defined steady state of the coupled system (see stability analysis in Appendix A 2 a).

Importantly, in Eq. (13), we can clearly observe the modifications that arise with respect to a single optical cavity, where one would have $\bar{a} = \alpha_{\text{las}} \sqrt{2\kappa_a} / [\kappa_a + \gamma_a + i\tilde{\Delta}_a]$, due to the coupling to the Fano mirror and due to dispersive and dissipative optomechanical couplings. The coupling via $\tilde{\mathcal{G}}$ to the Fano resonance modifies the effective environment coupling of the cavity as well as the effective resonance frequency.

2. Linearized Langevin equations

We now linearize the Langevin equations (8) around this semiclassical steady state (13), keeping terms only up to the first order in the fluctuations (see Appendix A 2 b for a discussion of the validity of this approximation),

$$\begin{aligned}\delta \dot{\hat{a}} &= -(i\tilde{\Delta}_a + \tilde{\kappa}_a + \gamma_a) \delta \hat{a} + i\sqrt{2}\tilde{g}_a \delta \hat{q} - i\tilde{\mathcal{G}} \delta \hat{d} \\ &\quad + \sqrt{2\tilde{\kappa}_a} \hat{a}_{\text{in,L}} + \sqrt{2\gamma_a} \hat{a}_{\text{in,R}}, \\ \delta \dot{\hat{d}} &= -(i\tilde{\Delta}_d + \tilde{\kappa}_d) \delta \hat{d} + i\sqrt{2}\tilde{g}_d \delta \hat{q} - i\tilde{\mathcal{G}} \delta \hat{a} + \sqrt{2\tilde{\kappa}_d} \hat{a}_{\text{in,L}}, \\ \delta \dot{\hat{q}} &= \Omega_{\text{mec}} \delta \hat{p}, \\ \delta \dot{\hat{p}} &= -\Omega_{\text{mec}} \delta \hat{q} - \Gamma_{\text{mec}} \delta \hat{p} + \sum_c \sqrt{2}(\tilde{g}_{\text{mec},c} \delta \hat{c}^\dagger + \tilde{g}_{\text{mec},c}^* \delta \hat{c}) \\ &\quad + c_X \sqrt{2\hat{X}_{\text{in,L}}} + c_P \sqrt{2\hat{P}_{\text{in,L}}} + \sqrt{\Gamma_{\text{mec}}} \hat{\xi}.\end{aligned}\quad (14)$$

We have defined the effective optomechanical couplings

$$\begin{aligned}\tilde{g}_a &= g_a^\omega \bar{a} + i g_a^\kappa \left(\bar{a} - \frac{\alpha_{\text{las}}}{\sqrt{2\kappa_a}} \right) + i g^{\kappa, \text{sym}} \bar{d}, \\ \tilde{g}_d &= g_d^\omega \bar{d} + i g_d^\kappa \left(\bar{d} - \frac{\alpha_{\text{las}}}{\sqrt{2\kappa_d}} \right) + i g^{\kappa, \text{sym}} \bar{a}, \\ \tilde{g}_{\text{mec},a} &= g_a^\omega \bar{a} - i g_a^\kappa \frac{\alpha_{\text{las}}}{\sqrt{2\kappa_a}} + i g^{\kappa, \text{asym}} \bar{d}, \\ \tilde{g}_{\text{mec},d} &= g_d^\omega \bar{d} - i g_d^\kappa \frac{\alpha_{\text{las}}}{\sqrt{2\kappa_d}} - i g^{\kappa, \text{asym}} \bar{a},\end{aligned}\quad (15)$$

the effective couplings of the mechanical resonator to the left optical environment

$$c_X = -\sum_c \frac{g_c^\kappa}{\sqrt{\kappa_c}} \text{Im}(\bar{c}), \quad c_P = \sum_c \frac{g_c^\kappa}{\sqrt{\kappa_c}} \text{Re}(\bar{c}), \quad (16)$$

and the quadratures of the optical input noises $\hat{X}_{\text{in},\mu} = \frac{1}{\sqrt{2}}(\hat{a}_{\text{in},\mu}^\dagger + \hat{a}_{\text{in},\mu})$ and $\hat{P}_{\text{in},\mu} = \frac{i}{\sqrt{2}}(\hat{a}_{\text{in},\mu}^\dagger - \hat{a}_{\text{in},\mu})$. Each effective optomechanical coupling defined in Eqs. (15) is divided into three parts: the dispersive coupling contribution, the dissipative coupling contribution, and a cross contribution [see Eq. (9)], due to the combination of the dissipative optomechanical effects and the coupling of the mirror mode and cavity mode to the same bath. In the limit $\lambda, \kappa_d \rightarrow 0$, we recover the results for a standard Fabry-Pérot cavity with both dispersive and dissipative optomechanical effects [34].

Finally, we linearize the input-output relation (10) and get

$$\begin{aligned}\hat{a}_{\text{out,L}}(t) &= \hat{a}_{\text{in,L}}(t) - \sum_c \sqrt{2\tilde{\kappa}_c} \delta \hat{c}(t) - (c_P - i c_X) \delta \hat{q}(t), \\ \hat{a}_{\text{out,R}}(t) &= \hat{a}_{\text{in,R}}(t) - \sqrt{2\gamma_a} \delta \hat{a}(t).\end{aligned}\quad (17)$$

3. Solution in the frequency domain

To determine the properties of this complex system, which will be analyzed in Sec. III, we solve the Langevin equations for $\delta \hat{a}$, $\delta \hat{d}$, $\delta \hat{q}$ [Eqs. (14)] in the frequency domain. The full solution is given in Appendix A 3. Here, we present the solution for the mechanical position fluctuations together with the relevant susceptibilities

$$\begin{aligned}\chi_{\text{mec,eff}}^{-1}[\omega] \delta \hat{q} &= \sum_{\mu,c} (\tilde{g}_{\text{mec},c}^* C_\mu^c[\omega] + \tilde{g}_{\text{mec},c} C_\mu^c[-\omega]^*) \hat{X}_{\text{in},\mu} \\ &\quad + i \sum_{\mu,c} (\tilde{g}_{\text{mec},c}^* C_\mu^c[\omega] - \tilde{g}_{\text{mec},c} C_\mu^c[-\omega]^*) \hat{P}_{\text{in},\mu} \\ &\quad + c_X \sqrt{2\hat{X}_{\text{in,L}}} + c_P \sqrt{2\hat{P}_{\text{in,L}}} + \sqrt{\Gamma_{\text{mec}}} \hat{\xi}.\end{aligned}\quad (18)$$

We have defined

$$\begin{aligned}C_L^a[\omega] &= \frac{i\sqrt{2\tilde{\kappa}_d} \tilde{\mathcal{G}} - \sqrt{2\tilde{\kappa}_d} \chi_d^{-1}[\omega]}{(\tilde{\Omega}_+ - \omega)(\tilde{\Omega}_- - \omega)}, \\ C_R^a[\omega] &= \frac{-\sqrt{2\gamma_a} \chi_a^{-1}[\omega]}{(\tilde{\Omega}_+ - \omega)(\tilde{\Omega}_- - \omega)}, \\ C_L^d[\omega] &= \frac{i\sqrt{2\tilde{\kappa}_a} \tilde{\mathcal{G}} - \sqrt{2\tilde{\kappa}_a} \chi_a^{-1}[\omega]}{(\tilde{\Omega}_+ - \omega)(\tilde{\Omega}_- - \omega)}, \\ C_R^d[\omega] &= \frac{i\sqrt{2\gamma_d} \tilde{\mathcal{G}}}{(\tilde{\Omega}_+ - \omega)(\tilde{\Omega}_- - \omega)},\end{aligned}\quad (19)$$

with the optical susceptibilities $\chi_a^{-1}[\omega] = \tilde{\kappa}_a + \gamma_a + i(\tilde{\Delta}_a - \omega)$ and $\chi_d^{-1}[\omega] = \tilde{\kappa}_d + i(\tilde{\Delta}_d - \omega)$.

The effective mechanical susceptibility $\chi_{\text{mec,eff}}$ can be written

$$\chi_{\text{mec,eff}}^{-1}[\omega] = \chi_{\text{mec,0}}^{-1}[\omega] + \chi_{\text{opt}}^{-1}[\omega], \quad (20)$$

where $\chi_{\text{mec,0}}[\omega] = \Omega_{\text{mec}}(\Omega_{\text{mec}}^2 - \omega^2 - i\omega\Gamma_{\text{mec}})^{-1}$ is the mechanical susceptibility of the bare resonator and $\chi_{\text{opt}}[\omega]$ the optical contribution to the susceptibility, which reads as

$$\chi_{\text{opt}}^{-1}[\omega] = -2 \sum_c (\tilde{g}_{\text{mec},c}^* C_q^c[\omega] + \tilde{g}_{\text{mec},c} C_q^c[-\omega]^*), \quad (21)$$

with

$$\begin{aligned} C_q^a[\omega] &= -i \frac{\chi_d^{-1}[\omega] \tilde{g}_a - i\tilde{G} \tilde{g}_d}{(\tilde{\Omega}_+ - \omega)(\tilde{\Omega}_- - \omega)}, \\ C_q^d[\omega] &= -i \frac{\chi_a^{-1}[\omega] \tilde{g}_d - i\tilde{G} \tilde{g}_a}{(\tilde{\Omega}_+ - \omega)(\tilde{\Omega}_- - \omega)}. \end{aligned} \quad (22)$$

These susceptibilities and their constituents deriving from different contributions of the dynamics will play an important role in the characterization of the optomechanical response of the device in Sec. III.

D. Studied devices

To give concrete examples and illustrate some of the properties of this complex optomechanical setup, we choose three sets of parameters, given in Table I: (i) the experimental device from Ref. [25] (see reference for details about obtaining the parameters and confirming the optomechanical-coupling strengths by other methods), (ii) a device with identical optical modes, i.e., $\delta_\Delta = \delta_\kappa = 0$, and (iii) a device⁴ with $\delta_\Delta = \delta_\kappa \lambda / \sqrt{\tilde{\kappa}_a \tilde{\kappa}_d}$.

All three devices are in the strong-optical-coupling regime (see Fig. 2 for a summary of the possible parameter regimes) and the effective “−” mode hence characterizes the physics of all three devices, while the highly damped “+” mode can be disregarded in the interpretation of the results. More precisely, devices (i) and (ii) are in the regime $|\tilde{G}| > |\delta_\kappa|, |\delta_\Delta|, \tilde{\kappa}_a, \tilde{\kappa}_d$ and, therefore, the effective modes “−” and “+” are very different from modes a and d , both in terms of frequency and loss rate. On the other hand, device (iii) is less strongly coupled in the sense that $|\delta_\kappa|, |\delta_\Delta|, \tilde{\kappa}_a > |\tilde{G}| > \tilde{\kappa}_d$, such that only the loss rate $\tilde{\kappa}_-$ is strongly modified. The parameters from (ii) and (iii) are inspired from (i) but modified to reach the effective resolved-sideband regime $\tilde{\kappa}_- \ll \Omega_{\text{mec}}$ (see also

the discussion in the end of Sec. II B 1), and such that $\tilde{\kappa}_-^{(ii)} = \tilde{\kappa}_-^{(iii)}$. Furthermore, to make it easier to reach the effective resolved-sideband regime and to enable ground-state cooling at room temperature, we choose state-of-the-art mechanical parameters $Q_{\text{mec}} = 1.4 \times 10^8$ and $\Omega_{\text{mec}}/2\pi = 1.3$ MHz from a SiN two-dimensional (2D) phononic crystal membrane [39]. But similar numbers could be achieved with InGaP-based mechanics [40], which is fully compatible with the microcavity from Ref. [25].

The frequency and loss rates of the mirror mode can be engineered by changing the photonic crystal pattern (lattice constant, hole radius) [19,35], which makes it possible to realize the conditions $\delta_\Delta = \delta_\kappa = 0$ and $\delta_\Delta = \delta_\kappa \lambda / \sqrt{\tilde{\kappa}_a \tilde{\kappa}_d}$ for devices (ii) and (iii). In addition, in order to reach the effective resolved-sideband regime, we need to identify appropriate damping rates γ_a for the cavity-environment coupling via the right mirror. For device (ii), we have $\tilde{\kappa}_-^{(ii)} \simeq \gamma_a/2$ (see Sec. II B 2), meaning that we need to take $\gamma_a \ll \Omega_{\text{mec}}$. While this might be challenging to achieve in specific microcavity setups of the type of Ref. [25] (where in practice it would need to include not only the transmission through the right mirror, but also all other losses like absorption or scattering), Device (ii) still constitutes an intriguing alternative setting to device (iii). For device (iii), we have the weaker constraint $\tilde{\kappa}_-^{(iii)} \simeq \gamma_a \tilde{\kappa}_d / 2\tilde{\kappa}$ (see Sec. II B 2), so by taking $\tilde{\kappa}_a \gg \tilde{\kappa}_d$ we obtain a device reaching the resolved-sideband regime with parameters for γ_a that are realistic for experimental realizations as in Ref. [25]. Indeed, with a highly reflective right mirror, such as a distributed Bragg reflector, one can achieve a very low transmission of around 10 ppm and ideally get total losses (transmission through the right mirror, absorption, and scattering) of 20 ppm. This would give a realistic value of $\gamma_a/2\pi \simeq 600$ MHz for device (iii).

The optomechanical couplings in devices (ii) and (iii) were decreased by four orders of magnitude compared to device (i). While this might deviate from expected values for currently realized microcavities, it ensures that those effectively sideband-resolved devices are in the linear regime (Sec. II C) and hence fulfill the stability criteria of Appendix A 2 a. In device (iii), g_d^κ was further decreased to match the decrease in $\tilde{\kappa}_d$ compared to device (ii). In Sec. V, we show how larger, and possibly even more realistic values for the optomechanical couplings, can allow for reaching the effective strong- and ultrastrong-coupling regimes.

Finally, in the following, we call “standard device” (denoted with superscript std) a canonical optomechanical setup with identical frequency-independent mirrors and the same sideband resolution as devices (ii) and (iii), namely, $\kappa_a^{\text{std}} = \gamma_a^{\text{std}} = \tilde{\kappa}_-^{(ii)}/2$, no mirror mode d , and only a dispersive optomechanical coupling g_a^ω .

III. OPTOMECHANICAL PROPERTIES

In this section, we study the optical and mechanical properties of the setup that can be measured in experiments so as to find signatures of the different optomechanical parameter regimes. We provide expressions to fit experimental data and determine the parameters characterizing the device.

⁴Reference [16] studies a different case. First, there are no optomechanical effects on the Fano mode and no dissipative optomechanical effects on the cavity mode in [16]. Second, the cavity and mirror modes in [16] are detuned by $\delta_\Delta = \lambda \sqrt{\kappa_a / \kappa_d}$, which comes from an assumption the authors made in their transfer matrix modeling, amounting to enforcing $\tilde{\Delta}_d \simeq \tilde{\Delta}_-$ and given their parameters (especially the free spectral range), they focus on longer cavities and their κ_d is a lot closer to the mechanical frequency compared to the values we consider in the following. While this choice of parameters is not specifically addressed in this work, it can however be covered by our model.

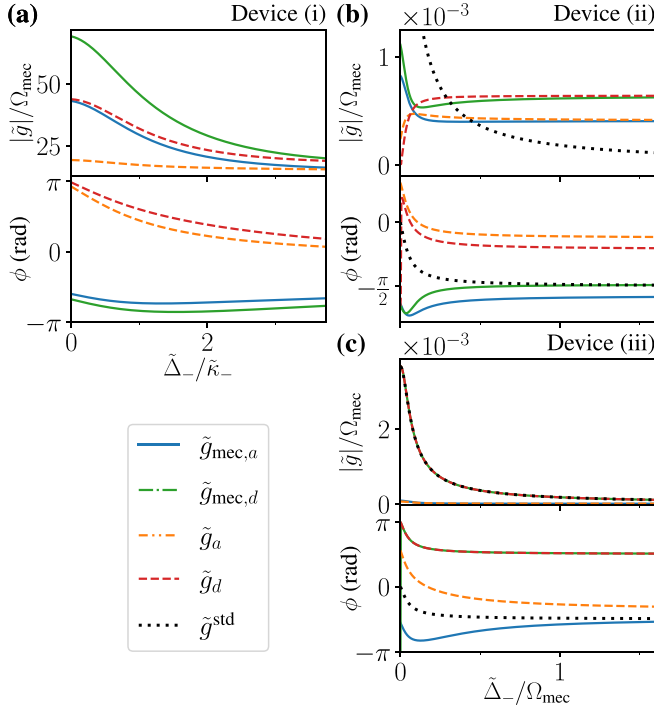


FIG. 3. Effective couplings [Eq. (15)] as functions of detuning for (a) device (i), (b) device (ii), and (c) device (iii). The couplings are complex numbers and the top panels show the absolute values of the couplings while the bottom panels show the phase $\tilde{g} = |\tilde{g}|e^{i\phi}$. The dotted black line corresponds to the effective coupling $\tilde{g}^{\text{std}} = g_a \bar{a}$ of a standard optomechanical device with the same sideband resolution as devices (ii) and (iii). The parameters are given in Table I.

A. Effective optomechanical couplings

The values of the effective optomechanical couplings, Eq. (15), vary a lot depending on the system's parameters. First, they are all proportional to α_{las} and therefore increase like the square root of the input laser power P_{las} . For purely dispersive optomechanics, namely, $g_a^{\kappa} = g_d^{\kappa} = 0$, one gets $\tilde{g}_c = \tilde{g}_{\text{mec},c} = g_c^{\omega} \bar{c}$. In this case, like in standard optomechanics, each coupling strength is simply enhanced by the square root of the average photon number in the corresponding mode $c = a, d$. However, the picture is more complicated for purely dissipative coupling. Even in the simple case $g_a^{\omega} = g_d^{\omega} = g_d^{\kappa} = 0$, \tilde{g}_a and $\tilde{g}_{\text{mec},a}$ are different while $\tilde{g}_d = -\tilde{g}_{\text{mec},d} \neq 0$ since $g^{\kappa, \text{asym}} = g^{\kappa, \text{sym}} = \frac{1}{2} \sqrt{\frac{\kappa_d}{\kappa_a}} g_a^{\kappa}$.

In Fig. 3, we show how the (complex-valued) couplings change with the “−”-mode detuning $\tilde{\Delta}_-$ for each device. The change in their phases directly originates from the change of phase in \bar{a} and \bar{d} due to the modification of $\tilde{\Delta}_a$ and $\tilde{\Delta}_d$ [see Eq. (13)]. We see that device (i) is in the ultrastrong-coupling regime $|\tilde{g}| > \Omega_{\text{mec}}$ as determined in Ref. [40], while devices (ii) and (iii) are not, which is due to our choice of single-photon optomechanical-coupling strengths (see Sec. II D and Table I). For a standard optomechanical device with only dispersive optomechanical coupling and without mirror mode d [dotted black line in Figs. 3(b) and 3(c)], the optomechanical coupling is $\tilde{g}_a = \tilde{g}_{\text{mec},a} = g_a^{\omega} \bar{a} \equiv \tilde{g}^{\text{std}}$. Since, in this case, there is a single effective coupling, the phase of \tilde{g}^{std} does not matter

and \tilde{g}^{std} can always be made real by changing the laser phase (in α_{las}). This is clearly not the case for device (ii) as there are four distinct effective couplings and some relative phases will always remain. Conversely, for device (iii), the effective optomechanical coupling of the mirror mode dominates, and since $\tilde{g}_d \simeq \tilde{g}_{\text{mec},d}$, it behaves effectively like a standard device: the curves for $|\tilde{g}_d|$, $|\tilde{g}_{\text{mec},d}|$ and $|\tilde{g}^{\text{std}}|$ are superimposed in Fig. 3(c).

B. Mean optical response

The mean steady-state optical output of the system can be measured in an experiment, especially the intensity transmission and reflection coefficients $T(\omega_{\text{las}}) = |t(\omega_{\text{las}})|^2$ and $R(\omega_{\text{las}}) = |r(\omega_{\text{las}})|^2$. Here, we have denoted $t = \langle \hat{b}_{\text{out},R} \rangle / \langle \hat{b}_{\text{in},L} \rangle$ the amplitude transmission coefficient, from left to right, since we have $\langle \hat{b}_{\text{in},R} \rangle = 0$, and the amplitude reflection coefficient $r = \langle \hat{b}_{\text{out},L} \rangle / \langle \hat{b}_{\text{in},L} \rangle$. Using the input-output relation (10), we obtain

$$t = -\sqrt{2\gamma_a} \frac{\bar{a}}{\alpha_{\text{las}}} = -\sqrt{2\gamma_a} C_L^a[0],$$

$$r = 1 - \sum_c \sqrt{2\tilde{\kappa}_c} \frac{\bar{c}}{\alpha_{\text{las}}} = 1 - \sum_c \sqrt{2\tilde{\kappa}_c} C_L^c[0], \quad (23)$$

with the steady-state amplitudes given in Eq. (13) and the coefficient C_L^c defined in Eqs. (19). With this, the intensity transmission becomes

$$T = \frac{2\gamma_a}{D} (\sqrt{2\tilde{\kappa}_a} \tilde{\Delta}_d - \sqrt{2\tilde{\kappa}_d} \tilde{\Delta}_a)^2, \quad (24)$$

with

$$D = |\tilde{\Omega}_-|^2 |\tilde{\Omega}_+|^2 = (\tilde{\Delta}_-^2 + \tilde{\kappa}_-^2)(\tilde{\Delta}_+^2 + \tilde{\kappa}_+^2). \quad (25)$$

The intensity transmission is modulated by the average mechanical displacement in the following way:

$$\frac{dT}{d\tilde{q}} = \sqrt{2} \sum_c \left(-g_c^{\omega} \frac{\partial T}{\partial \tilde{\Delta}_c} + g_c^{\kappa} \frac{\partial T}{\partial \tilde{\kappa}_c} \right) \quad (26)$$

(see Appendix B for the full expressions of the derivatives).

In Fig. 4, we plot the constituents of Eq. (26), namely, the partial derivatives associated with each kind of optomechanical coupling. We first notice that the main response takes place around $\tilde{\Delta}_- = 0$, that is when the laser is close to resonance with the “−” effective optical mode. We have normalized $\partial T / \partial x$, with $x = \tilde{\Delta}_a, \tilde{\Delta}_d, \tilde{\kappa}_a, \tilde{\kappa}_d$, by the maximum transmission of the optical setup T_{max} . The motivation for this is that the devices have very different γ_a and, in particular, device (ii) barely transmits any light since the coupling to the right environment is many orders of magnitude smaller than the couplings to the left environment (see Table I). Figure 4 shows that the transmission of device (i) is affected very little by the mechanics since it is very far from the effective sideband-resolved regime, unlike for the other devices. We also see that, for devices (i) and (ii), all the derivatives have similar magnitudes though different shapes, while, for device (iii) in Fig. 4(c), the derivatives with respect to the Fano-mirror-mode quantities largely dominate, as already observed for the effective optomechanical couplings. For a standard optomechanical device, the only relevant derivative is $\partial T^{\text{std}} / \partial \tilde{\Delta}_a$,

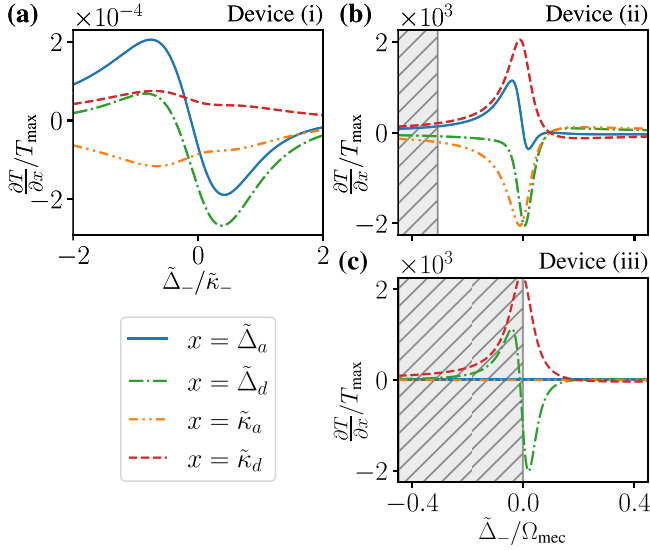


FIG. 4. Optical response to the variation of different detunings and bath couplings as a function of the “-”-mode detuning for (a) device (i), (b) device (ii), and (c) device (iii). We have plotted each partial derivative from Eq. (26). The hatched areas indicate detunings for which the respective devices are unstable due to heating [see Fig. 5(a) and Appendix A 2 a]. The parameters are given in Table I.

which is similar to $\partial T/\partial \tilde{\Delta}_d$ for device (iii) [dashed-dotted green line in Fig. 4(c)], with two off-resonant sidebands [33]. The main difference between the two is that $\partial T^{\text{std}}/\partial \tilde{\Delta}_a$ is an odd function of the detuning $\tilde{\Delta}_a$, while $\partial T/\partial \tilde{\Delta}_d$ is not exactly an odd function of $\tilde{\Delta}_-$ due to the coupling between the optical modes. Similarly, there is an asymmetry in the dominant dissipative derivative $\partial T/\partial \tilde{\kappa}_d$ while dissipative derivatives would be even functions of the detuning in the absence of coupling between the optical modes [33].

C. Mechanical response

After studying how the mechanical motion impacts the mean optical transmission, we now do the opposite and analyze the effects of the optomechanical couplings on the mechanical motion. To do so, we write the effective mechanical susceptibility, Eq. (20), in the usual form for a harmonic oscillator [1], that is $\chi_{\text{mec,eff}}[\omega] = \Omega_{\text{mec}}(\Omega_{\text{mec}}^{\text{eff}}[\omega]^2 - \omega^2 - i\omega\gamma^{\text{eff}}[\omega])^{-1}$, identifying the effective mechanical frequency $\Omega_{\text{mec}}^{\text{eff}}[\omega] = \Omega_{\text{mec}} + \delta\Omega_{\text{mec}}[\omega]$ and damping rate $\gamma^{\text{eff}}[\omega] = \Gamma_{\text{mec}} + \Gamma_{\text{opt}}[\omega]$, where we have defined the optical contribution to the mechanical damping rate and the mechanical frequency shift, in the limit $\delta\Omega_{\text{mec}} \ll \Omega_{\text{mec}}$:

$$\begin{aligned}\Gamma_{\text{opt}}[\omega] &= -\frac{\Omega_{\text{mec}}}{\omega} \text{Im}(\chi_{\text{opt}}^{-1}[\omega]), \\ \delta\Omega_{\text{mec}}[\omega] &= \frac{1}{2} \text{Re}(\chi_{\text{opt}}^{-1}[\omega]).\end{aligned}\quad (27)$$

We have plotted $\delta\Omega_{\text{mec}}[\Omega_{\text{mec}}]$ and $\Gamma_{\text{opt}}[\Omega_{\text{mec}}]$ for device (ii) (in blue) and device (iii) (in orange) as a function of the detuning $\tilde{\Delta}_-$ in Fig. 5(a). They give the frequency shift and optical contributions to the mechanical damping rate in the weak-optomechanical-coupling regime $|\tilde{g}| < \Omega_{\text{mec}}, \tilde{\kappa}_-$, which is relevant for the laser powers considered here (see

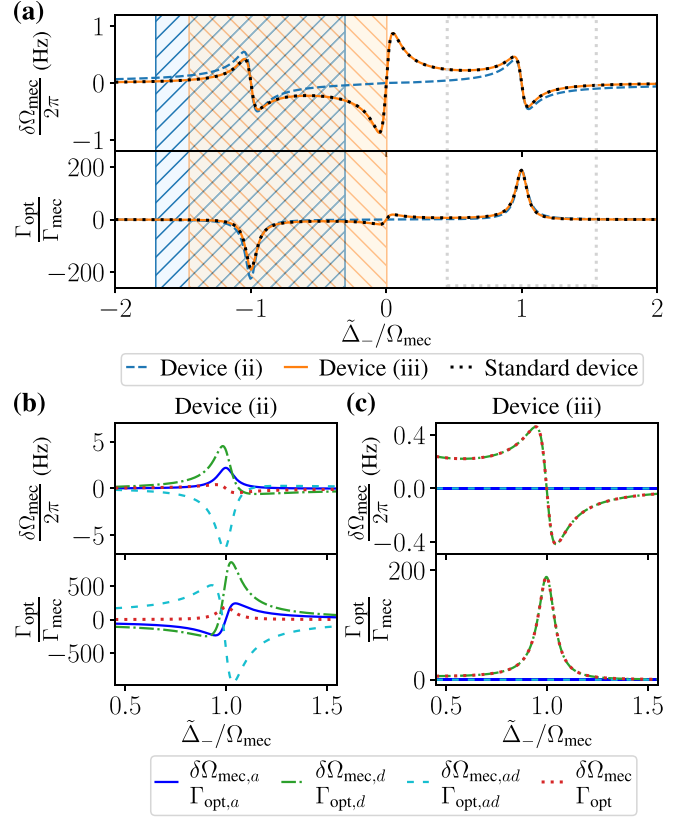


FIG. 5. (a) Mechanical frequency shift $\delta\Omega_{\text{mec}}$ (top panel) and optical contribution to the mechanical damping rate Γ_{opt} (bottom panel) as a function of the detuning $\tilde{\Delta}_-$ for devices (ii) and (iii). The plots were obtained by evaluating Eqs. (27) at $\omega = \Omega_{\text{mec}}$. The hatched areas indicate detunings for which the respective devices are unstable due to the heating. The dotted black lines represent a standard resolved-sideband optomechanical device where the laser power has been adjusted to get a similar cooling on the red sideband. (b), (c) Components of the mechanical frequency shift $\delta\Omega_{\text{mec}}$ (top panels) and optical contribution to the mechanical damping rate Γ_{opt} (bottom panels) as a function of the detuning $\tilde{\Delta}_-$ around the red sideband [gray dotted box in (a)] for device (ii) and device (iii) at $\omega = \Omega_{\text{mec}}$ [see Eq. (28)]. The parameters are given in Table I.

values in Table I and Fig. 3 for $|\tilde{g}|/\Omega_{\text{mec}}$). We see frequency shifts on both sidebands, i.e., around $\tilde{\Delta}_- = \pm\Omega_{\text{mec}}$, which are similar to the ones of a standard optomechanical device, indicated by the dotted black line. Similarly, we observe the expected peaks in Γ_{opt} indicating, respectively, cooling on the red sideband and heating on the blue sideband. For the considered laser powers, this heating effect is large enough to make the system unstable (hatched areas) (see stability analysis in Appendix A 2 a for more details). This means that while the theory developed in this article, and in particular the linearization from Sec. II C, is not valid in those hatched areas, it still predicts an overall negative mechanical damping rate.⁵ All in all, both devices behave like a standard optomechanical device. However, while the behavior of device (iii) is really

⁵See, e.g., Ref. [1] for a discussion of this lasing effect, that we will not study in this work, for a standard optomechanical device.

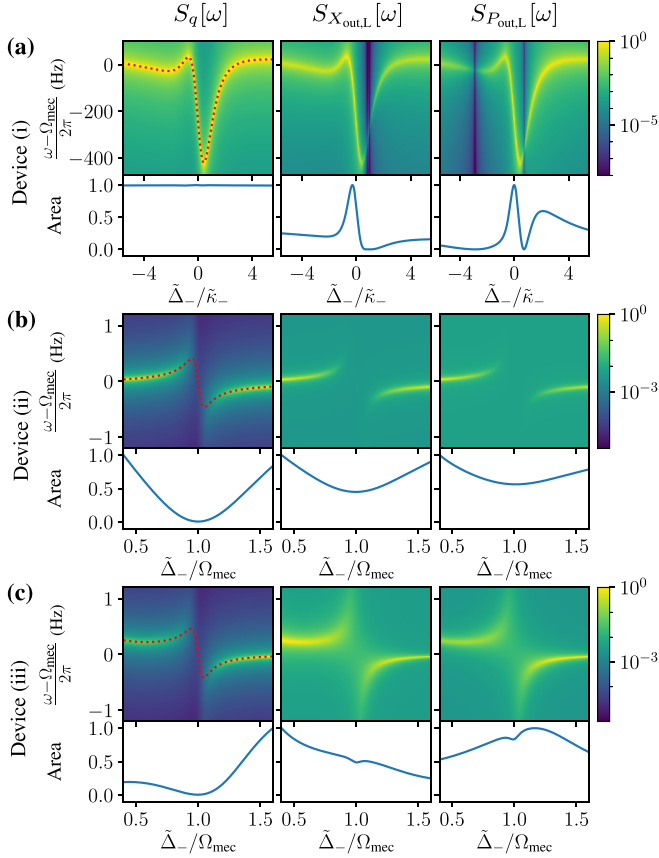


FIG. 6. Noise power spectra of (a) device (i), (b) device (ii), and (c) device (iii). Upper row of each panel: Noise power spectrum of the mechanical position $S_q[\omega]$ and light output quadratures on the left side $S_{X_{out,L}}[\omega]$ and $S_{P_{out,L}}[\omega]$ as functions of the effective detuning $\hat{\Delta}_-$ and of the frequency ω . The dotted red line shows the mechanical frequency shift $\delta\Omega_{mec}[\Omega_{mec}]$. Lower row of each panel: Area corresponding to the integral over ω of the corresponding spectrum in the upper row. All the plotted quantities have been normalized by their maximum values; all parameters are given in Table I.

identical to the one of a standard device, device (ii) has a different behavior around zero detuning.

We would like to note that device (i) is not sideband resolved, therefore, the relevant detuning scale for the atypical frequency shift $\delta\Omega_{mec}[\Omega_{mec}]$ is $\tilde{\kappa}_-$ and not Ω_{mec} (discussed in detail in Ref. [25]). The damping rate $\Gamma_{opt}[\Omega_{mec}]$ of device (i) is negligible, therefore, there is no significant cooling or heating. These findings are reflected in the noise power spectrum of the mechanical position [Fig. 6(a)], discussed in Sec. III D.

In order to better understand the contribution of the different optical modes to the mechanical damping rate and frequency shift, we now split the optical contribution to the mechanical susceptibility, using Eqs. (21) and (22), into

$$\chi_{opt}^{-1}[\omega] = \chi_{opt,a}^{-1}[\omega] + \chi_{opt,d}^{-1}[\omega] + \chi_{opt,ad}^{-1}[\omega], \quad (28)$$

with

$$\chi_{opt,a}^{-1}[\omega] = -2i \frac{\tilde{g}_{mec,a}^* \tilde{g}_a \chi_d^{-1}[\omega]}{(\tilde{\Omega}_+ - \omega)(\tilde{\Omega}_- - \omega)} + (\omega \rightarrow -\omega)^*,$$

$$\begin{aligned} \chi_{opt,d}^{-1}[\omega] &= -2i \frac{\tilde{g}_{mec,d}^* \tilde{g}_d \chi_a^{-1}[\omega]}{(\tilde{\Omega}_+ - \omega)(\tilde{\Omega}_- - \omega)} + (\omega \rightarrow -\omega)^*, \\ \chi_{opt,ad}^{-1}[\omega] &= -2 \frac{(\tilde{g}_{mec,a}^* \tilde{g}_d + \tilde{g}_{mec,d}^* \tilde{g}_a) \tilde{\mathcal{G}}}{(\tilde{\Omega}_+ - \omega)(\tilde{\Omega}_- - \omega)} + (\omega \rightarrow -\omega)^*. \end{aligned} \quad (29)$$

The notation $\dots + (\omega \rightarrow -\omega)^*$ means that we replace ω by $-\omega$ in \dots and take the complex conjugate. We can apply the same decomposition to the damping rate and the mechanical frequency shift, $\Gamma_{opt} = \Gamma_{opt,a} + \Gamma_{opt,d} + \Gamma_{opt,ad}$ and $\delta\Omega_{mec} = \delta\Omega_{mec,a} + \delta\Omega_{mec,d} + \delta\Omega_{mec,ad}$, by applying the definitions (27) to the components of χ_{opt}^{-1} . From the effective coupling perspective, $\chi_{opt,c}^{-1}[\omega]$ is a pure contribution from the optical mode $c = a, d$, but note that \tilde{g}_c and $\tilde{g}_{mec,c}$ contain some cross terms in $g^{k,asym}$ or $g^{k,sym}$ [see Eqs. (15)]. However, in the limit of purely dispersive optomechanical couplings, namely $g_a^k, g_d^k \rightarrow 0$, the factor $\tilde{g}_{mec,c}^* \tilde{g}_c$ becomes $(g_c^\omega |\bar{c}|)^2$.

These three components of $\delta\Omega_{mec}[\Omega_{mec}]$ and $\Gamma_{opt}[\Omega_{mec}]$ are plotted around the red sideband in Figs. 5(b) and 5(c). For device (ii) in Fig. 5(b), the components have similar magnitudes and partially cancel each other out, giving rise to a lower total quantity (dotted red line). On the other hand, Fig. 5(c) confirms that the dominant contribution to the optomechanics in device (iii) comes from the effective d coupling since the dashed-dotted green line representing the d contribution is superimposed with the dotted red line of the total quantity.

D. Quadrature output power spectra

In experiments, one typically measures the noise power spectrum of the light transmitted ($\hat{a}_{out,R}$) or reflected ($\hat{a}_{out,L}$) by the cavity, for instance, with a homodyne detection scheme [25], with the goal to also deduct information about the mechanics. Using the input-output relations (17), we compute the power spectra of the quadratures of the light leaking out of the cavity, defined by⁶

$$S_{Q_{out,\mu}}[\omega] = \int_{-\infty}^{+\infty} \frac{d\omega'}{2\pi} \langle \hat{Q}_{out,\mu}[\omega] \hat{Q}_{out,\mu}[\omega'] \rangle, \quad (30)$$

with $Q = X, P$ and $\mu = L, R$. Here, $\hat{X}_{out,\mu} = (\hat{a}_{out,\mu} + \hat{a}_{out,\mu}^\dagger)/\sqrt{2}$ and $\hat{P}_{out,\mu} = (\hat{a}_{out,\mu} - \hat{a}_{out,\mu}^\dagger)/i\sqrt{2}$ are the position and momentum quadratures of the output light. We obtain

$$\begin{aligned} S_{X_{out,L}}[\omega] &= S_{X_{in,L}}[\omega] + 2c_P^2 S_q[\omega] + 4\sqrt{\tilde{\kappa}_a \tilde{\kappa}_d} S_{X_a X_d}[\omega] \\ &\quad + \sum_c (2\tilde{\kappa}_c S_{X_c}[\omega] + 4\sqrt{\tilde{\kappa}_c} c_P S_{X_c q}[\omega]), \\ S_{P_{out,L}}[\omega] &= S_{P_{in,L}}[\omega] + 2c_X^2 S_q[\omega] + 4\sqrt{\tilde{\kappa}_a \tilde{\kappa}_d} S_{P_a P_d}[\omega] \\ &\quad + \sum_c (2\tilde{\kappa}_c S_{P_c}[\omega] + 4\sqrt{\tilde{\kappa}_c} c_X S_{P_c q}[\omega]) \\ S_{X_{out,R}}[\omega] &= S_{X_{in,R}}[\omega] + 2\gamma_a S_{X_a}[\omega], \\ S_{P_{out,R}}[\omega] &= S_{P_{in,R}}[\omega] + 2\gamma_a S_{P_a}[\omega], \end{aligned} \quad (31)$$

⁶Note that the spectra relevant for measurements such as homodyne detection are the symmetrized spectra. Due to the noise model considered in this work, we have $S_{Q_{out,\mu}}[-\omega] = S_{Q_{out,\mu}}[\omega]$ and the result of Eq. (30) hence is identical to the symmetrized version (see Appendix C).

with $S_Q[\omega]$ the spectrum of $\delta\hat{Q}$ for $Q = X_c, P_c, q$ and the input vacuum noise spectra $S_{X_{in,\mu}}[\omega] = S_{P_{in,\mu}}[\omega] = \frac{1}{2}$. We have also defined the cross terms

$$S_{Q_1 Q_2}[\omega] = \frac{1}{2} \int_{-\infty}^{+\infty} \frac{d\omega'}{2\pi} \langle \delta\hat{Q}_1[\omega] \delta\hat{Q}_2[\omega'] + \delta\hat{Q}_2[\omega] \delta\hat{Q}_1[\omega'] \rangle. \quad (32)$$

These spectra can be computed from the solution of the Langevin equations (14) (see analytical expressions in Appendix C). In particular, for the mechanical position spectrum $S_q[\omega]$, using Eq. (18), we get

$$S_q[\omega] = |\chi_{\text{mec}}^{\text{eff}}[\omega]|^2 (S_{\text{th}}[\omega] + S_{\text{om}}[\omega]), \quad (33)$$

where $S_{\text{th}}[\omega] \simeq 2\Gamma_{\text{mec}}\bar{n}_{\text{mec}}$ is the thermal noise spectrum in the high mechanical temperature limit ($\hbar\Omega_{\text{mec}} \ll k_B T_{\text{mec}}$) relevant here (see Ref. [41] for a more general expression). Finally,

$$S_{\text{om}}[\omega] = \frac{1}{2} \left| \sum_c 2\tilde{g}_{\text{mec},c}^* C_L^c[\omega] + \sqrt{2}(c_X - ic_P) \right|^2 + \frac{1}{2} \left| \sum_c 2\tilde{g}_{\text{mec},c}^* C_R^c[\omega] \right|^2 \quad (34)$$

is the noise power spectrum due to the optomechanical effects.

In the high mechanical temperature limit, the part of the noise power spectra coming from the optical environments (vacuum noise) is negligible compared to the thermal noise from the mechanical environment. As a consequence the spectrum given in Eq. (33) can be approximated by $S_q[\omega] \simeq 2\Gamma_{\text{mec}}\bar{n}_{\text{mec}}|\chi_{\text{mec}}^{\text{eff}}[\omega]|^2$. The noise spectra $S_{X_{\text{out},\mu}}[\omega]$ and $S_{P_{\text{out},\mu}}[\omega]$ are proportional to the factor $\Gamma_{\text{mec}}|\chi_{\text{mec}}^{\text{eff}}[\omega]|^2$ as well and, therefore, exhibit a peak at the effective mechanical frequency, as shown in Fig. 6 for all three devices (the effective mechanical frequency is indicated by the dotted red line). However, the noise spectrum $S_{Q_{\text{out},\mu}}[\omega]$, with $Q = X, P$, in general also has additional frequency-dependent factors and hence its area $\int \frac{d\omega}{2\pi} S_{Q_{\text{out},\mu}}[\omega]$ does not give direct access to the mechanical fluctuations $\langle \delta\hat{q}^2 \rangle = \int_{-\infty}^{+\infty} \frac{d\omega}{2\pi} S_q[\omega]$ (see Appendix C for details on how to compute $\langle \delta\hat{q}^2 \rangle$ from the optical output spectra).

For the devices we consider here, the frequency dependence of these factors can be neglected on the range of values of ω relevant for mechanical features, such that $\int \frac{d\omega}{2\pi} (S_{Q_{\text{out},\mu}}[\omega] - S_{Q_{\text{in},\mu}}[\omega]) \propto \langle \delta\hat{q}^2 \rangle$. But this proportionality factor is strongly dependent on the detuning $\tilde{\Delta}_-$, which explains the difference between the area plots of optical and mechanical noise power spectra (lower row of each panel) in Fig. 6. In particular, for device (i), these additional detuning-dependent contributions have an important effect that should not be confused with optomechanical cooling. In Fig. 6(a), both $S_{X_{\text{out},L}}[\omega]$ and $S_{P_{\text{out},L}}[\omega]$ exhibit dark blue lines at distinct values of $\tilde{\Delta}_-$, where the optical spectra are suppressed. This is in qualitative agreement with the experimental measurements [25]. Note that this is a pure optical effect, as can be seen from the area of the mechanical spectrum $S_q[\omega]$, $\int \frac{d\omega}{2\pi} S_q[\omega]$, in the lower-left panel of Fig. 6(a), which is constant. Conversely,

for the other two devices, the cooling observed as a dip of the area of $S_q[\omega]$ around $\tilde{\Delta}_- = \Omega_{\text{mec}}$ is still visible on top of the optical contributions to the areas of $S_{X_{\text{out},\mu}}[\omega]$ and $S_{P_{\text{out},\mu}}[\omega]$. In Fig. 6(b), for device (ii), the optical contributions manifest as an approximately constant shift of the area while for device (iii), in Fig. 6(c), the cooling dip is visible, even though only faintly, on top of the $\tilde{\Delta}_-$ -dependent optical features.

IV. BACK-ACTION COOLING

After having demonstrated the general properties of the optomechanical Fano-mirror system, we now focus on a widely used application, namely, cooling of the mechanical resonator using optomechanical back-action. It is well known that this cooling scheme allows to bring *sideband-resolved* standard optomechanical systems into the mechanical ground state [4,5,42]. In this section, we show that similar achievements are possible for our system, even if $\kappa_d, \kappa_a + \gamma_a \gg \Omega_{\text{mec}}$ [device (ii)] or $\kappa_d, \kappa_a, \gamma_a \gg \Omega_{\text{mec}}$ [device (iii)]. This is possible since these devices are in the *effective* sideband-resolved regime $\tilde{\kappa}_- \lesssim \Omega_{\text{mec}}$.

We start this section by analyzing the underlying cooling mechanisms in the weak-coupling regime, where the optomechanical-coupling strengths are significantly smaller than the mechanical frequency and the (effective) optical loss rates, which is the case for the laser powers given in Table I.

A. Stokes and anti-Stokes scattering processes

The steady-state phonon number in the mechanical fluctuations,

$$\bar{n}_{\text{fin}} = \frac{1}{2} (\langle \delta\hat{q}^2 \rangle + \langle \delta\hat{p}^2 \rangle - 1), \quad (35)$$

results in the weak-optomechanical-coupling limit, from the competition between the Stokes and anti-Stokes scattering processes, which respectively create and annihilate phonons in the mechanical resonator. The respective rates A_+ and A_- of those processes are given by $A_{\pm} = \frac{1}{2} S_{FF}[\mp\Omega_{\text{mec}}]$ [1], where $S_{FF}[\omega] = \int_{-\infty}^{+\infty} \frac{d\omega'}{2\pi} \langle \delta\hat{F}[\omega] \delta\hat{F}[\omega'] \rangle$ is the noise power spectrum of the optical back-action on the mechanical resonator,

$$\delta\hat{F} = \sum_c \sqrt{2}(\tilde{g}_{\text{mec},c} \delta\hat{c}^\dagger + \tilde{g}_{\text{mec},c}^* \delta\hat{c}) + c_X \sqrt{2} \hat{X}_{\text{in},L} + c_P \sqrt{2} \hat{P}_{\text{in},L}, \quad (36)$$

obtained from the steady-state solution of the Langevin equations [see the last two lines of Eq. (14)]. In the weak-coupling limit, the effect of the mechanics on the optics can be neglected and we compute $S_{FF}[\omega]$ by solving the Langevin equations (14) for the optics only [see also Eq. (2)]. This yields $\delta\hat{c}[\omega] = C_L^c[\omega] \hat{a}_{\text{in},L}[\omega] + C_R^c[\omega] \hat{a}_{\text{in},R}[\omega]$ and, hence,

$$A_{\pm} = \left| \sum_c \left(\tilde{g}_{\text{mec},c}^* C_L^c[\mp\Omega_{\text{mec}}] - \frac{g_c^* \alpha_{\text{las}}^*}{\sqrt{2}\kappa_c} C_L^c[0] \right) \right|^2 + \left| \sum_c \tilde{g}_{\text{mec},c}^* C_R^c[\mp\Omega_{\text{mec}}] \right|^2. \quad (37)$$

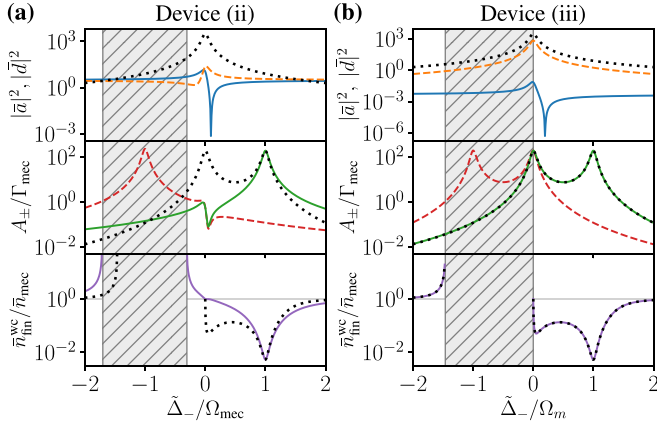


FIG. 7. Optomechanical cooling in the weak-coupling limit and resolved-sideband regime $\tilde{\kappa}_- \ll \Omega_{\text{mec}}$. We show results for (a) device (ii) and (b) device (iii) (see parameters in Table I). Top panels: average photon numbers in the cavity ($|a|^2$, solid blue) and in the Fano mirror ($|d|^2$, dashed orange); center panels: anti-Stokes (solid green) and Stokes (dashed red) rates; bottom panels: obtained average phonon number in the mechanical fluctuations (solid purple), the gray line indicates the thermal phonon number \bar{n}_{mec} . All functions are plotted in dependence of the detuning between the laser and the effective “-” mode. The dotted black lines correspond to the result for a standard optomechanical device with the same sideband resolution (we have only plotted A_- in the middle panel), and the hatched areas indicate detunings for which the system is unstable due to heating.

From these rates, we identify the characteristics of the *effective phonon bath* created by the optical part of the setup [1,17]: its effective damping rate $\Gamma_{\text{opt}}^{\text{wc}} = A_- - A_+$ [coinciding with $\Gamma_{\text{opt}}[\Omega_{\text{mec}}]$ from Fig. 5(a) in this limit] and its effective average phonon number $\bar{n}_{\text{opt}} = A_+/\Gamma_{\text{opt}}$. As a result of the coupling to this effective phonon bath created by the optical setup, the steady-state phonon number in the mechanical fluctuations is then given by

$$\bar{n}_{\text{fin}}^{\text{wc}} = \frac{\Gamma_{\text{mec}}\bar{n}_{\text{mec}} + \Gamma_{\text{opt}}^{\text{wc}}\bar{n}_{\text{opt}}}{\Gamma_{\text{mec}} + \Gamma_{\text{opt}}^{\text{wc}}}. \quad (38)$$

In the middle panels of Fig. 7, we see that the Stokes rate A_+ (dashed red) and anti-Stokes rate A_- (solid green) exhibit peaks at the blue and red sidebands, respectively, corresponding to heating and cooling. Device (ii) [Fig. 7(a)] has similar features as a standard resolved-sideband optomechanical device but with a slight asymmetry between A_+ and A_- , which explains why Γ_{opt} is not an odd function of the detuning in Fig. 5(a). For both devices, the weak-optomechanical-coupling approximation gives a good estimate of \bar{n}_{fin} [see purple diamonds in Figs. 8(a) and 8(b)]. Figure 7 confirms the observation from Fig. 5(a) that, despite the large parameter differences between devices (ii) and (iii), their behavior on both sidebands is very similar, almost identical to the one of a standard device (dotted black line). Differences mainly occur close to zero detuning, which is not relevant for cooling applications.

The effective optomechanical couplings $\tilde{g}_{\text{mec},c}$ are proportional to the laser drive amplitude α_{las} [see Eqs. (13) and (15)], such that A_{\pm} and $\Gamma_{\text{opt}}^{\text{wc}}$ are proportional to the laser power

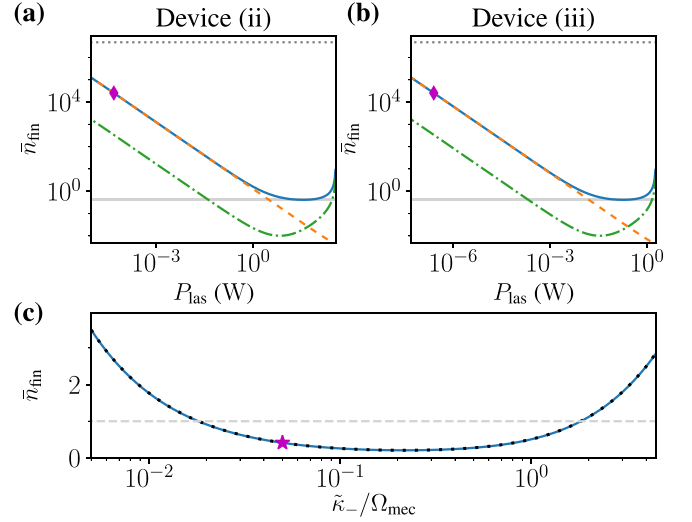


FIG. 8. Steady-state phonon number in the mechanical fluctuations [Eq. (35)]. Results as function of the laser power at $\tilde{\Delta}_- = \Omega_{\text{mec}}$ are shown for (a) device (ii) and (b) device (iii) at room temperature, $T_{\text{mec}} = 300$ K (solid blue line), and at cryogenic temperature, $T_{\text{mec}} = 4$ K (dashed-dotted green line). For the room-temperature case, the dotted gray line indicates the thermal phonon number, the dashed orange line the weak-coupling approximation [Eq. (38)], and the solid gray line the minimum reachable phonon number. The purple diamonds indicate the laser powers used in the other figures as indicated in Table I. (c) Minimum steady-state phonon number in the mechanical fluctuations (minimized on $\tilde{\Delta}_-$ and P_{las}) as function of the sideband resolution, where $\tilde{\kappa}_-$ is tuned via $\tilde{\kappa}_d$ and $\tilde{\Delta}_d$. The solid blue line was obtained with a device differing from device (iii) only by the laser power with $\delta_{\Delta} = \delta_{\kappa}\lambda/\sqrt{\tilde{\kappa}_d\tilde{\kappa}_-}$. The purple star indicates devices (ii) and (iii) and the dotted black line corresponds to the minimum \bar{n}_{fin} for a standard optomechanical device, with the ideal parameters $\gamma_a = \kappa_a = \tilde{\kappa}_-/2$. The dashed gray line indicated the ground-state cooling threshold. All other parameters are given in Table I.

as well. Consequently, increasing P_{las} brings the steady-state phonon number $\bar{n}_{\text{fin}}^{\text{wc}}$ [Eq. (38)] closer to \bar{n}_{opt} . Since $\bar{n}_{\text{opt}} \simeq 6.3 \times 10^{-4} \ll 1$ for devices (ii) and (iii), ground-state cooling is expected to be possible. However, the weak-coupling approximation typically breaks down well before \bar{n}_{fin} reaches \bar{n}_{opt} . We therefore need to study the steady-state phonon number beyond the weak-coupling limit, as will be done in the following subsection IV B.

B. Ground-state cooling

In the limit where the weak-optomechanical-coupling approximation fails, the phonon number in the mechanical fluctuations \bar{n}_{fin} can be computed from Eq. (35) by solving the Lyapunov equation for the system in the steady state, as detailed in Appendix A 4.

We plot \bar{n}_{fin} obtained with optomechanical cooling as a function of the laser power for devices (ii) and (iii) in Figs. 8(a) and 8(b), where we choose the detuning $\tilde{\Delta}_- = \Omega_{\text{mec}}$ due to the weak-coupling results from Sec. IV A. We see that both Fano-mirror devices (ii) and (iii) can achieve ground-state cooling, both for cryogenic temperature, at

$T_{\text{mec}} = 4$ K (dashed-dotted green lines) and for room temperature (solid blue lines). The phonon number reaches a minimum of $\bar{n}_{\text{fin}} \simeq 0.41$ at room temperature, while a lower phonon occupation $\bar{n}_{\text{fin}} \simeq 0.01$ can be reached at cryogenic temperature. In Appendix D, we additionally show that energy equipartition $\langle \delta \hat{q}^2 \rangle \simeq \langle \delta \hat{p}^2 \rangle$ is satisfied close to the lowest phonon occupation. As shown by the dashed orange line for the room-temperature case, the weak-coupling approximation eventually breaks down at large laser powers.

Even though devices (ii) and (iii) have very different optical parameters for modes a and d , Figs. 8(a) and 8(b) are almost identical, showing that the key optical parameter determining the cooling limit is the effective sideband resolution $\tilde{\kappa}_{-}/\Omega_{\text{mec}}$. Therefore, we have also plotted the minimum phonon number as a function of the sideband resolution in Fig. 8(c), showing that devices differing from device (iii) in Table I only by the tunable laser power (solid blue line) have identical cooling performances as a standard optomechanical device (dotted black line). This further confirms the results from Figs. 5 and 7, namely, that around the red sideband, this complex engineered device behaves like a simple standard resolved-sideband optomechanical device, where the ideal sideband resolution has been achieved thanks to the Fano-mirror engineering.

Evidently, the mechanical frequency and quality factor also play a major role in determining the cooling limit. Room-temperature ground-state cooling is made possible here by the large mechanical frequency and high mechanical quality factor (see Table I). In addition, note that we have assumed the drive laser to be shot noise limited, that is in a coherent state, while in an experiment, one would need to account for the laser phase noise and make sure it does not prevent the setup from reaching the mechanical ground state [43,44]. Finally, the only difference between Figs. 8(a) and 8(b) is the laser power at which the minimum \bar{n}_{fin} is reached. Device (ii) requires a laser power two orders of magnitude larger than device (iii). This comes from the difference in the optical parameters, in particular giving rise to different effective optomechanical couplings g^{ω} and different laser frequencies giving $\tilde{\Delta}_{-} = \Omega_{\text{mec}}$. Therefore, identical laser powers correspond to different input photon rates $P_{\text{las}}/\hbar\omega_{\text{las}}$.

V. TOWARDS NONLINEAR OPTOMECHANICS

In this section we show that a system, as realized by a microcavity with a frequency-dependent Fano mirror, can reach the effective resolved-sideband, strong- and ultrastrong-coupling regimes simultaneously. To that end, we introduce two additional model systems, Devices (iv) and (v), with parameters that are close to situations that can be experimentally achieved with microcavities [35,40] (see Table II). These systems are based on state-of-the-art mechanical parameters [39] and, like device (iii), fulfill the condition $\delta_{\Delta} = \delta_{\kappa}\lambda/\sqrt{\tilde{\kappa}_a\tilde{\kappa}_d}$. It allows them to be in the effective resolved-sideband regime with $\tilde{\kappa}_{-} < \Omega_{\text{mec}}$ obtained from Eq. (3).

Compared to the previous sections, where the device parameters were based on Table I, we now chose more realistic optomechanical couplings for modes a and d for experimental microcavity implementations like in Ref. [25] [device (i)]. Concretely, comparing to Ref. [25] we only

TABLE II. Experimentally achievable devices in the effective resolved-sideband regime ($\tilde{\kappa}_{-}/\Omega_{\text{mec}} < 1$), thanks to the condition $\delta_{\Delta} = \delta_{\kappa}\lambda/\sqrt{\tilde{\kappa}_a\tilde{\kappa}_d}$, going toward both the strong- ($g^{\omega} > \tilde{\kappa}_{-}$) and ultrastrong- ($g^{\omega} > \Omega_{\text{mec}}$) coupling regimes. See Table I for the description of the parameters. Like for devices (ii) and (iii), the effective dissipative coupling g^{κ}_{-} is negligible, $g^{\kappa}_{-} \ll g^{\omega}_{-}$ (see Sec. II B 1).

Parameter	Device (iv)	Device (v)
<i>Optical modes</i>		
$\delta_{\Delta}/2\pi$ (Hz)	1.13×10^{13}	1.97×10^{13}
$\gamma_a/2\pi$ (Hz)	1.00×10^9	6.00×10^8
$\tilde{\kappa}_a/2\pi$ (Hz)	1.00×10^{13}	1.00×10^{13}
$\tilde{\kappa}_d/2\pi$ (Hz)	3.25×10^9	1.08×10^9
$\lambda/2\pi$ (Hz)	4.09×10^{11}	4.09×10^{11}
<i>Mechanical mode</i>		
$\Omega_{\text{mec}}/2\pi$ (Hz)	1.3×10^6	1.3×10^6
$\Gamma_{\text{mec}}/2\pi$ (Hz)	9.3×10^{-3}	9.3×10^{-3}
Q_{mec}	1.4×10^8	1.4×10^8
<i>Single-photon optomechanical couplings</i>		
$g_a^{\omega}/\Omega_{\text{mec}}$	0.065	0.65
$g_d^{\omega}/\Omega_{\text{mec}}$	-0.14	-1.4
$g_a^{\kappa}/\Omega_{\text{mec}}$	0.060	0.60
$g_d^{\kappa}/\Omega_{\text{mec}}$	2.1×10^{-4}	4.2×10^{-4}
<i>Effective optical “-” mode</i>		
$\tilde{\kappa}_{-}/\Omega_{\text{mec}}$	0.25	0.05
$g^{\omega}_{-}/\Omega_{\text{mec}}$	-0.14	-1.4
$g^{\omega}_{-}/\tilde{\kappa}_{-}$	-0.56	-28

decrease the optomechanical couplings by a factor 10 for device (iv) and keep the same values as in device (i) for device (v). Note that we further decreased g_d^{κ} to reflect the smaller value of $\tilde{\kappa}_d$ in devices (iv) and (v) compared to device (i). Despite the stronger optomechanical coupling, the modeling from Sec. II A remains valid for devices (iv) and (v), in particular for the calculation of the effective optical modes from Sec. II A 2 since $\tilde{\kappa}_a, \tilde{\kappa}_d \gg g_a^{\omega}, g_d^{\omega}, g_a^{\kappa}, g_d^{\kappa}$. We can therefore make quantitative statements about the relevant effective coupling parameters, given in the last section of Table II.

Here, we find that device (iv) is close to reaching both the effective strong-coupling regime $|g^{\omega}_{-}| > \tilde{\kappa}_{-}$ and the effective ultrastrong-coupling regime $|g^{\omega}_{-}| > \Omega$. Indeed, we see in the last rows of Table II that $|g^{\omega}_{-}| = 0.56\tilde{\kappa}_{-}$ and $|g^{\omega}_{-}| = 0.14\Omega$, compared to the devices in Table I, where these parameters typically differ by several orders of magnitude. The situation is even more favorable for device (v) reaching both the effective strong-coupling regime $|g^{\omega}_{-}| = 28\tilde{\kappa}_{-}$ and the effective ultrastrong-coupling regime $|g^{\omega}_{-}| = 1.4\Omega$. The required parameters of the mirror mode, ω_d and κ_d , can be realized by engineering the photonic crystal pattern and the right-hand-side cavity loss rate γ_a is achievable with distributed Bragg reflectors. Our work thus predicts that reaching simultaneously the resolved-sideband, strong- and ultrastrong-coupling regimes is within reach of optical microcavities with a frequency-dependent mirror such as a photonic crystal, paving the way for the experimental exploration of the nonlinear regime of cavity quantum optomechanics.

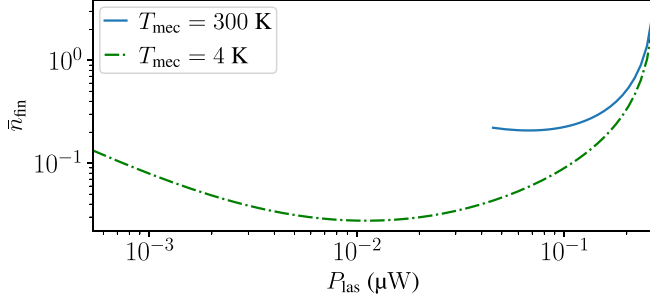


FIG. 9. Steady-state phonon number in the mechanical fluctuations [Eq. (35)] as function of the laser power at $\tilde{\Delta}_- = \Omega_{\text{mec}}$ for device (iv). The curves have been plotted on the laser power range where the device's dynamics can be linearized (Sec. II C).

In general, the theoretical approach to analyze the *dynamics* presented here, namely, the linearization from Sec. II C, does not apply for this strong-coupling regime. However, for strong enough laser powers, the dynamics of device (iv) can be linearized since $|\tilde{c}|^2 \gg \langle \delta \hat{c}^\dagger \delta \hat{c} \rangle$ (see also Appendix A 2). Hence, for those laser powers, we are able to show results for the phonon number that can be reached via optomechanical cooling, using the theoretical framework given in Sec. II. The result is shown in Fig. 9, displaying the steady-state phonon number in the mechanical fluctuations at $\tilde{\Delta}_- = \Omega_{\text{mec}}$, evidencing that ground-state cooling is possible with this device too (see Appendix D for the energy equipartition). The linearization is valid for a smaller range of laser powers at room temperature (solid blue line) than at cryogenic temperature (dashed-dotted green line) since the thermal fluctuations of the mechanics, which give rise to optical fluctuations due to the optomechanical couplings, increase with temperature. An analysis of the full nonlinear dynamics of devices (iv) and (v) is postponed to future work.

VI. CONCLUSION

Our work highlights that optomechanical systems with a Fano mirror can reach an *effective* resolved-sideband regime. Thanks to the strong interaction between the two optical modes, i.e., the Fano and the cavity modes, a significant reduction of the effective optical linewidth is achievable by matching the resonance frequencies and loss rates of these two modes. Therefore, sideband-based ground-state cooling of the mechanics is expected to become possible even for a microcavity with high optical losses $\tilde{\kappa}_a \gg \Omega_{\text{mec}}$ and at room temperature.

We have established a complex but versatile theoretical model, taking into account both dispersive and dissipative optomechanical couplings for a cavity with one frequency-dependent mirror. The full analytical description makes it possible to investigate different effects separately, namely, couplings not relevant to a chosen specific experimental setup can easily be set to zero. Furthermore, the cavity output spectrum is not trivially related to the noise spectrum of the mechanical resonator and our work gives the required expressions to make this inference. We therefore expect this model to be a useful tool for all similar or analogous setups, where coupled optical modes interact with mechanical modes. This can

be applied to various systems ranging from optomechanical cavities studied here to magnon modes coupled to mechanical deformation [45,46], molecular optomechanics [47], or cavity-enhanced chemistry, etc. (see, e.g., Refs. [48,49]).

Finally, we have demonstrated that this complex optomechanical system can be mapped to a canonical optomechanical setting with ideal coupling and loss parameters. Importantly, this shows that the advantage of strong single-photon coupling of microcavities and the designed reduced loss rates of effective optical modes due to a Fano mirror are a promising route for implementing both strong coupling and ultrastrong coupling in optomechanics, paving the way for nonlinear quantum optomechanics.

ACKNOWLEDGMENTS

We thank L. Du for helpful comments on the manuscript. We acknowledge financial support by the Knut och Alice Wallenberg stiftelse through project Grant No. 2022.0090 (J.S., W.W.), the Wallenberg Center for Quantum Technology (A.C.), as well as through individual Wallenberg Academy Fellow grants (J.S., W.W.). Also funding from the Swedish Vetenskapsrådet via Projects No. 2018-05061 (J.M., J.S.), No. 2019-04946, and No. 2019-00390 (W.W.), and the QuantERA project (C'MON-QSENS!) are gratefully acknowledged.

APPENDIX A: DYNAMICS

In this Appendix, we provide derivations and technical background for the (linearized) Langevin equations and the resulting Lyapunov equations, which are used throughout the main paper to describe the dynamics of the optomechanical system.

1. Derivation of the Langevin equations

From the microscopic model described in Sec. II B 1, we derive the dynamics of the system in the Heisenberg picture,

$$\begin{aligned} \dot{\hat{b}}_{\omega,L} = & -i\omega\hat{b}_{\omega,L} - \sqrt{\frac{\kappa_a}{\pi}} \left(1 + \frac{g_a^\kappa}{\sqrt{2}\kappa_a} \hat{q} \right) \hat{a} \\ & - \sqrt{\frac{\kappa_d}{\pi}} \left(1 + \frac{g_d^\kappa}{\sqrt{2}\kappa_d} \hat{q} \right) \hat{d}, \end{aligned} \quad (\text{A1a})$$

$$\dot{\hat{b}}_{\omega,R} = -i\omega\hat{b}_{\omega,R} - \sqrt{\frac{\gamma_a}{\pi}} \hat{a}, \quad (\text{A1b})$$

$$\begin{aligned} \dot{\hat{a}} = & -i\omega_a\hat{a} - i\lambda\hat{d} + ig_a^\omega\sqrt{2}\hat{q}\hat{a} \\ & + \sqrt{\frac{\kappa_a}{\pi}} \left(1 + \frac{g_a^\kappa}{\sqrt{2}\kappa_a} \hat{q} \right) \int d\omega \hat{b}_{\omega,L} \\ & + \sqrt{\frac{\gamma_a}{\pi}} \int d\omega \hat{b}_{\omega,R}, \end{aligned} \quad (\text{A1c})$$

$$\begin{aligned} \dot{\hat{d}} = & -i\omega_d\hat{d} - i\lambda\hat{a} + ig_d^\omega\sqrt{2}\hat{q}\hat{d} \\ & + \sqrt{\frac{\kappa_d}{\pi}} \left(1 + \frac{g_d^\kappa}{\sqrt{2}\kappa_d} \hat{q} \right) \int d\omega \hat{b}_{\omega,L}, \end{aligned} \quad (\text{A1d})$$

$$\dot{\hat{q}} = \Omega_{\text{mec}}\hat{p}, \quad (\text{A1e})$$

$$\dot{\hat{p}} = -\Omega_{\text{mec}}\hat{q} + \sum_c \left(g_c^\omega \sqrt{2}\hat{c}^\dagger \hat{c} - i \frac{g_c^\kappa}{\sqrt{2\pi\kappa_c}} \right) \times \int d\omega (\hat{c}^\dagger \hat{b}_{\omega,L} - \hat{b}_{\omega,L}^\dagger \hat{c}). \quad (\text{A1f})$$

We formally integrate Eqs. (A1a) and (A1b) with respect to an initial time $t_0 < t$, and insert the obtained expression in the other equations of the system (A1). Defining the input fields

$$\hat{b}_{\text{in},\mu}(t) = \frac{1}{\sqrt{2\pi}} \int d\omega \hat{b}_{\omega,\mu}(t_0) e^{-i\omega(t-t_0)}, \quad (\text{A2})$$

with $\mu = L, R$, and following the same procedure as in Ref. [36], we obtain the Langevin equations (8). We have added the terms $-\Gamma_{\text{mec}}\hat{p}$ and $\sqrt{\Gamma_{\text{mec}}}\hat{\xi}$ in the evolution of \hat{p} to take into account the thermal mechanical noise, assuming that $\Gamma_{\text{mec}} \ll \Omega_{\text{mec}}, g_a^\omega, g_a^\kappa, \gamma_a, \kappa_a, \kappa_d$.

The output fields are defined by taking a reference time in the future $t_1 > t$:

$$\hat{b}_{\text{out},\mu}(t) = \frac{1}{\sqrt{2\pi}} \int d\omega \hat{b}_{\omega,\mu}(t_1) e^{-i\omega(t-t_1)}. \quad (\text{A3})$$

Comparing the formal integration of Eqs. (A1a) with respect to t_0 and t_1 gives the input-output relations (10).

2. Validity of the linearization

For the linearized dynamics described in Sec. II C to be valid, two key conditions need to be fulfilled. First, we have assumed the existence of a well-defined stable classical steady-state solution of the nonlinear system of equations (13), which can be verified by applying the Routh-Hurwitz criterion (see below). Second, we have neglected terms at the second order in the fluctuations in the Langevin equations (14) and it needs to be guaranteed that the neglected terms are indeed sufficiently small. In the following, we do not discuss device (i) since the linearization for this device is valid for all the considered detunings due to the large effective optical losses $\tilde{\kappa}_- \gg g_c^\omega, g_c^\kappa, \Omega_{\text{mec}}$ (see Table I).

a. Stability of the system

We apply the Routh-Hurwitz criterion to determine whether the system, described by the Langevin equations (8), is stable for the studied parameters. Focusing on the equation for the quadratures and following the procedure described in Ref. [50], we construct the sequence $(r_k)_{0 \leq k \leq 6}$ based on the characteristic polynomial of A [Eq. (A10)], $\det(A - XI) = \sum_{k=0}^6 a_{-k} X^k$. If all the elements of this sequence have the same sign, then the system is stable. The elements are defined in the following way: $r_0 = T_0$, $r_1 = T_1$, and $r_k = T_k/T_{k-1}$ for $k = 2, \dots, 6$ with $T_0 = a_0$, $T_1 = a_1$, and $T_{k>1} = \det M_k$. Here, M_k is the $k \times k$ matrix with coefficients $(M_k)_{ij} = a_{2i-j}$ and we take $a_{2i-j} = 0$ if $2i-j$ is not between 0 and 6. In particular, $r_0 = 1$, $r_1 = 2(\gamma_a + \kappa_a + \kappa_d) + \Gamma_{\text{mec}}$, and $r_6 = a_6 = \det(A)$ but the full analytical expressions of the other coefficients are rather complex and not very informative. However, by evaluating numerically $r_{k>1}$ we can find that devices (ii) and (iii) have instabilities (see hatched regions in relevant plots of the main paper) which coincide very well with the places at which \bar{n}_{fin} becomes negative.

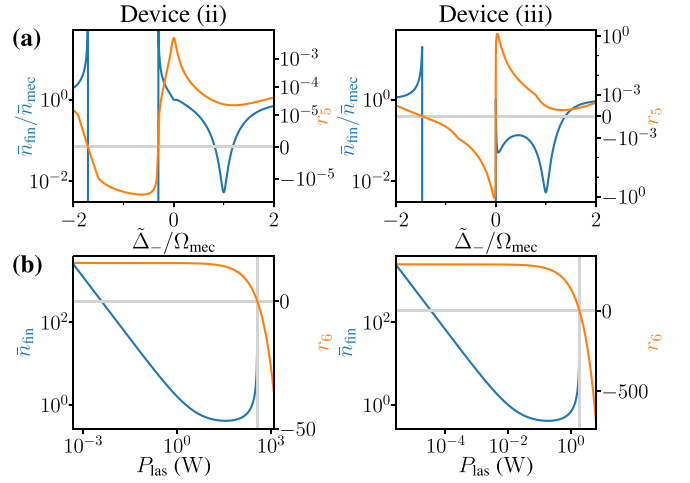


FIG. 10. Steady-state phonon number \bar{n}_{fin} (in blue, left axis) and relevant stability condition (in orange, right axis) as a function of (a) the detuning $\tilde{\Delta}_-$ and (b) the laser power P_{las} for devices (ii) and (iii). See Table I for the other parameters.

In particular, the instability regions in Figs. 4, 5(a), and 7 as a function of the detuning $\tilde{\Delta}_-$ for a fixed laser power coincide with negativities of r_5 [see Fig. 10(a)]. However, when the system is driven on the red sideband, at $\tilde{\Delta}_- = \Omega_{\text{mec}}$, the relevant criterion, namely, the first one to become negative, for the stability of the system as a function of the laser power is $r_6 = \det(A) > 0$, as illustrated in Fig. 10(b). Similar results are obtained for the other devices.

b. Negligibility of the second order in the fluctuations

We compare the fluctuations in the photon numbers $\langle \delta \hat{c}^\dagger \delta \hat{c} \rangle$, with the average photon numbers in the classical steady state $|\bar{c}|^2$ from Eq. (13), for both the cavity mode ($c = a$ in green) and mirror mode ($c = d$ in red) in Fig. 11. The photon-number fluctuations $\langle \delta \hat{c}^\dagger \delta \hat{c} \rangle$ are obtained by numerically solving the steady-state Lyapunov equations for the second-order moments (see Appendix A 4). While $|\bar{c}|^2$ is independent of the temperature T_{mec} , since thermal fluctuations average to zero, $\langle \delta \hat{c}^\dagger \delta \hat{c} \rangle$ decreases by several orders of magnitude when going from room temperature (dashed lines) to cryogenic temperature (dotted lines). Indeed, the thermal fluctuations in the mechanical resonator create optical fluctuations due to the optomechanical coupling; therefore, having a colder mechanical environment reduces these thermal fluctuations. Figures 11(a) and 11(b) correspond to the positive detuning part of Fig. 7 and it shows that apart from around $\bar{a} \approx 0$, which happens at $\omega_{\text{las}} = \omega_d - \sqrt{\tilde{\kappa}_d/\tilde{\kappa}_a}\lambda$ [see Eq. (13)], the linearization is valid for devices (ii) and (iii).

Figures 11(c)–11(e) show that, at $\tilde{\Delta}_- = \Omega_{\text{mec}}$, the linearization is valid if the laser power is sufficiently large for devices (ii)–(iv), which is the case in all figures presented in this paper. The laser powers used in most figures (see Table I) for devices (ii) and (iii) are indicated by the vertical dotted black line in Fig. 11(b). However, the linearization for device (v), in Fig. 11(f), is never valid, which is expected since this device is in the strong-coupling regime $g_-^\omega > \tilde{\kappa}_-$.

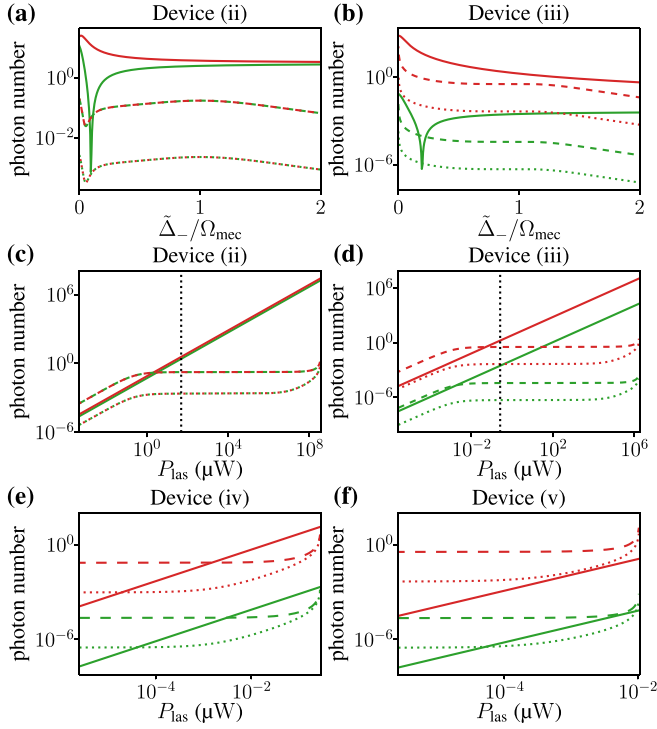


FIG. 11. Steady-state photon numbers, for the cavity mode in green and the mirror mode in red, in the classical steady state $|\bar{c}|^2$ (solid lines) and in the fluctuations $\langle \delta \hat{c}^\dagger \delta \hat{c} \rangle$ (dashed lines at $T_{\text{mec}} = 300$ K and dotted lines at $T_{\text{mec}} = 4$ K) as a function of (a), (b) the detuning $\tilde{\Delta}_-$ and (c)–(f) the laser power P_{las} (at $\tilde{\Delta}_- = \Omega_{\text{mec}}$) for the device indicated on top of each panel. The dotted vertical black lines in (c) and (d) indicate the laser powers used in all the figures where P_{las} is not on the x axis. See Table I for the other parameters of devices (ii) and (iii) and Table II for the parameters of devices (iv) and (v).

3. Solution of the linearized Langevin equations

In the frequency domain, using the convention $\hat{f}[\omega] = \int_{-\infty}^{+\infty} dt e^{i\omega t} \hat{f}(t)$ for the Fourier transform, the linearized Langevin equations (14) become

$$\begin{aligned} \chi_a^{-1}[\omega] \delta \hat{a} &= i\sqrt{2}\tilde{g}_a \delta \hat{q} - i\tilde{g}_d \delta \hat{a} + \sqrt{2\tilde{\kappa}_a} \hat{a}_{\text{in,L}} + \sqrt{2\gamma_a} \hat{a}_{\text{in,R}}, \\ \chi_d^{-1}[\omega] \delta \hat{d} &= i\sqrt{2}\tilde{g}_d \delta \hat{q} - i\tilde{g}_a \delta \hat{a} + \sqrt{2\tilde{\kappa}_d} \hat{a}_{\text{in,L}}, \\ \delta \hat{p} &= -i\frac{\omega}{\Omega_{\text{mec}}} \delta \hat{q}, \\ \chi_{\text{mec},0}^{-1}[\omega] \delta \hat{q} &= \sqrt{2} \sum_c (\tilde{g}_{\text{mec},c} \delta \hat{c}^\dagger + \tilde{g}_{\text{mec},c}^* \delta \hat{c}) + \sqrt{\Gamma_{\text{mec}}} \hat{\xi} \\ &\quad + c_X \sqrt{2} \hat{X}_{\text{in,L}} + c_P \sqrt{2} \hat{P}_{\text{in,L}}. \end{aligned} \quad (\text{A4})$$

The susceptibilities χ_a , χ_d , and $\chi_{\text{mec},0}$ are given in Sec. II C 3. From these equations, we obtain

$$\delta \hat{c} = \sqrt{2} C_q^c[\omega] \delta \hat{q} + C_L^c[\omega] \hat{a}_{\text{in,L}} + C_R^c[\omega] \hat{a}_{\text{in,R}}, \quad (\text{A5})$$

with the coefficients C^c defined in Eqs. (19) and (22). Then we get Eqs. (18) and (21) by putting Eq. (A5) in the last equation of (A4).

Furthermore, we can write each quadrature \hat{Q} , with $Q = X_a, P_a, X_d, P_d, q, p$, as

$$\delta \hat{Q}[\omega] = \sum_\eta c_\eta^Q[\omega] \hat{\eta}[\omega], \quad (\text{A6})$$

where we are summing over the input noises $\hat{\eta} = \hat{X}_{\text{in,L}}, \hat{P}_{\text{in,L}}, \hat{X}_{\text{in,R}}, \hat{P}_{\text{in,R}}, \hat{\xi}$, and we have defined the coefficients

$$\begin{aligned} c_{X_{\text{in},\mu}}^q[\omega] &= \chi_{\text{mec,eff}}[\omega] \sum_c (\tilde{g}_{\text{mec},c}^* C_\mu^c[\omega] + \tilde{g}_{\text{mec},c} C_\mu^c[-\omega]^*) \\ &\quad + \delta_{\mu,L} \chi_{\text{mec,eff}}[\omega] c_X \sqrt{2}, \\ c_{P_{\text{in},\mu}}^q[\omega] &= \chi_{\text{mec,eff}}[\omega] \sum_c i(\tilde{g}_{\text{mec},c}^* C_\mu^c[\omega] - \tilde{g}_{\text{mec},c} C_\mu^c[-\omega]^*) \\ &\quad + \delta_{\mu,L} \chi_{\text{mec,eff}}[\omega] c_P \sqrt{2}, \\ c_\xi^q[\omega] &= \chi_{\text{mec,eff}}[\omega] \sqrt{\Gamma_{\text{mec}}}, \\ c_\eta^p[\omega] &= -i\frac{\omega}{\Omega_{\text{mec}}} c_\eta^q[\omega], \\ c_{X_{\text{in},\mu}}^{X_c}[\omega] &= (C_q^c[\omega] + C_q^c[-\omega]^*) c_{X_{\text{in},\mu}}^q[\omega] \\ &\quad + \frac{C_\mu^c[\omega] + C_\mu^c[-\omega]^*}{2}, \\ c_{P_{\text{in},\mu}}^{X_c}[\omega] &= (C_q^c[\omega] + C_q^c[-\omega]^*) c_{P_{\text{in},\mu}}^q[\omega] \\ &\quad + i\frac{C_\mu^c[\omega] - C_\mu^c[-\omega]^*}{2}, \\ c_\xi^{X_c}[\omega] &= (C_q^c[\omega] + C_q^c[-\omega]^*) c_\xi^q[\omega], \\ c_{X_{\text{in},\mu}}^{P_c}[\omega] &= i(C_q^c[-\omega]^* - C_q^c[\omega]) c_{X_{\text{in},\mu}}^q[\omega] \\ &\quad + i\frac{C_\mu^c[-\omega]^* - C_\mu^c[\omega]}{2}, \\ c_{P_{\text{in},\mu}}^{P_c}[\omega] &= i(C_q^c[-\omega]^* - C_q^c[\omega]) c_{P_{\text{in},\mu}}^q[\omega] \\ &\quad + \frac{C_\mu^c[\omega] + C_\mu^c[-\omega]^*}{2}, \\ c_\xi^{P_c}[\omega] &= i(C_q^c[-\omega]^* - C_q^c[\omega]) c_\xi^q[\omega]. \end{aligned} \quad (\text{A7})$$

4. Evolution of the second-order moments

Due to the linearization in Sec. II C, the system is Gaussian. Therefore, the evolution of the second-order moments of the quadratures can be put in the form of a Lyapunov equation

$$\frac{dV}{dt} = AV + VA^T + B \quad (\text{A8})$$

for the covariance matrix V of the quadratures. The elements of the covariance matrix V are defined as

$$V_{ij} = \frac{1}{2} \langle \{Y_i, Y_j\} \rangle - \langle Y_i \rangle \langle Y_j \rangle, \quad (\text{A9})$$

with $\vec{Y} = (\delta \hat{X}_a, \delta \hat{P}_a, \delta \hat{X}_d, \delta \hat{P}_d, \delta \hat{q}, \delta \hat{p})$. We have defined the optical quadratures $\delta \hat{X}_a = (\delta \hat{a} + \delta \hat{a}^\dagger)/\sqrt{2}$, $\delta \hat{P}_a = (\delta \hat{a} - \delta \hat{a}^\dagger)/i\sqrt{2}$, $\delta \hat{X}_d = (\delta \hat{d} + \delta \hat{d}^\dagger)/\sqrt{2}$, and $\delta \hat{P}_d = (\delta \hat{d} - \delta \hat{d}^\dagger)/i\sqrt{2}$. The expressions of the matrices

A and B,

$$A = \begin{bmatrix} -\tilde{\kappa}_a - \gamma_a & \tilde{\Delta}_a & -\sqrt{\tilde{\kappa}_a \tilde{\kappa}_d} & \lambda & -2 \operatorname{Im}(\tilde{g}_a) & 0 \\ -\tilde{\Delta}_a & -\tilde{\kappa}_a - \gamma_a & -\lambda & -\sqrt{\tilde{\kappa}_a \tilde{\kappa}_d} & 2 \operatorname{Re}(\tilde{g}_a) & 0 \\ -\sqrt{\tilde{\kappa}_a \tilde{\kappa}_d} & \lambda & -\tilde{\kappa}_d & \tilde{\Delta}_d & -2 \operatorname{Im}(\tilde{g}_d) & 0 \\ -\lambda & -\sqrt{\tilde{\kappa}_a \tilde{\kappa}_d} & -\tilde{\Delta}_d & -\tilde{\kappa}_d & 2 \operatorname{Re}(\tilde{g}_d) & 0 \\ 0 & 0 & 0 & 0 & 0 & \Omega_{\text{mec}} \\ 2 \operatorname{Re}(\tilde{g}_{\text{mec},a}) & 2 \operatorname{Im}(\tilde{g}_{\text{mec},a}) & 2 \operatorname{Re}(\tilde{g}_{\text{mec},d}) & 2 \operatorname{Im}(\tilde{g}_{\text{mec},d}) & -\Omega_{\text{mec}} & -\Gamma_{\text{mec}} \end{bmatrix},$$

$$B = \begin{bmatrix} \tilde{\kappa}_a + \gamma_a & 0 & \sqrt{\tilde{\kappa}_a \tilde{\kappa}_d} & 0 & 0 & c_X \sqrt{\tilde{\kappa}_a} \\ 0 & \tilde{\kappa}_a + \gamma_a & 0 & \sqrt{\tilde{\kappa}_a \tilde{\kappa}_d} & 0 & c_P \sqrt{\tilde{\kappa}_a} \\ \sqrt{\tilde{\kappa}_a \tilde{\kappa}_d} & 0 & \tilde{\kappa}_d & 0 & 0 & c_X \sqrt{\tilde{\kappa}_d} \\ 0 & \sqrt{\tilde{\kappa}_a \tilde{\kappa}_d} & 0 & \tilde{\kappa}_d & 0 & c_P \sqrt{\tilde{\kappa}_d} \\ 0 & 0 & 0 & 0 & 0 & 0 \\ c_X \sqrt{\tilde{\kappa}_a} & c_P \sqrt{\tilde{\kappa}_a} & c_X \sqrt{\tilde{\kappa}_d} & c_P \sqrt{\tilde{\kappa}_d} & 0 & c_P^2 + c_X^2 + \Gamma_{\text{mec}}(2\bar{n}_{\text{mec}} + 1) \end{bmatrix}. \quad (\text{A10})$$

are obtained from the Langevin equations (14) and the correlation functions of the noise, Eqs. (12) and (11). Solving numerically the Lyapunov equation (A8) for the steady state, $A\bar{V} + \bar{V}A^T + B = 0$, gives access to, among other quantities, the phonon number in the mechanical fluctuations [Eq. (35)]

$$\bar{n}_{\text{lin}} = \frac{1}{2}(\bar{V}_{55} + \bar{V}_{66} - 1). \quad (\text{A11})$$

APPENDIX B: DETAILED ANALYTICAL EXPRESSIONS FOR THE MEAN OPTICAL RESPONSE

The optical response of the optomechanical system is discussed in Sec. III B. Here, we provide explicit analytical expressions, which are not given in Sec. III B.

The derivative of the intensity transmission T in Eq. (26) can be explicitly expressed as

$$\begin{aligned} \frac{\partial T}{\partial \tilde{\Delta}_a} &= -\frac{\partial D}{\partial \tilde{\Delta}_a} \frac{T}{D}, \\ \frac{\partial T}{\partial \tilde{\Delta}_d} &= -\frac{\partial D}{\partial \tilde{\Delta}_d} \frac{T}{D} + \frac{8\gamma_a}{D}(\tilde{\kappa}_a \tilde{\Delta}_d - \sqrt{\tilde{\kappa}_a \tilde{\kappa}_d} \lambda), \\ \frac{\partial T}{\partial \tilde{\kappa}_a} &= -\frac{\partial D}{\partial \tilde{\kappa}_a} \frac{T}{D} + \frac{4\gamma_a \tilde{\Delta}_d}{D} \left(\tilde{\Delta}_d - \sqrt{\frac{\tilde{\kappa}_d}{\tilde{\kappa}_a}} \lambda \right), \\ \frac{\partial T}{\partial \tilde{\kappa}_d} &= -\frac{\partial D}{\partial \tilde{\kappa}_d} \frac{T}{D} - \frac{4\gamma_a \lambda}{D} \left(\sqrt{\frac{\tilde{\kappa}_a}{\tilde{\kappa}_d}} \tilde{\Delta}_d - \lambda \right), \end{aligned} \quad (\text{B1})$$

with

$$\begin{aligned} \frac{\partial D}{\partial \tilde{\Delta}_a} &= 2\tilde{\Delta}_d(\tilde{\kappa}_a \tilde{\kappa}_d - \lambda^2) - 4\lambda \tilde{\kappa}_d \sqrt{\tilde{\kappa}_a \tilde{\kappa}_d} + 2(\tilde{\Delta}_d^2 + \tilde{\kappa}_d^2) \tilde{\Delta}_a, \\ \frac{\partial D}{\partial \tilde{\Delta}_d} &= 2\tilde{\Delta}_a(\tilde{\kappa}_a \tilde{\kappa}_d - \lambda^2) - 4\lambda(\tilde{\kappa}_a + \gamma_a) \sqrt{\tilde{\kappa}_a \tilde{\kappa}_d} \\ &\quad + 2(\tilde{\Delta}_a^2 + (\tilde{\kappa}_a + \gamma_a)^2) \tilde{\Delta}_d, \\ \frac{\partial D}{\partial \tilde{\kappa}_a} &= 2 \left[\tilde{\Delta}_d - \sqrt{\frac{\tilde{\kappa}_d}{\tilde{\kappa}_a}} \lambda \right] [\tilde{\Delta}_a \tilde{\kappa}_d + \tilde{\Delta}_d(\tilde{\kappa}_a + \gamma_a) - 2\lambda \sqrt{\tilde{\kappa}_a \tilde{\kappa}_d}], \\ \frac{\partial D}{\partial \tilde{\kappa}_d} &= 2 \left[\tilde{\Delta}_a - \sqrt{\frac{\tilde{\kappa}_a}{\tilde{\kappa}_d}} \lambda \right] [\tilde{\Delta}_a \tilde{\kappa}_d + \tilde{\Delta}_d(\tilde{\kappa}_a + \gamma_a) - 2\lambda \sqrt{\tilde{\kappa}_a \tilde{\kappa}_d}] \\ &\quad + 2\gamma_a(\lambda^2 + \gamma_a \tilde{\kappa}_d - \tilde{\Delta}_a \tilde{\Delta}_d). \end{aligned} \quad (\text{B2})$$

APPENDIX C: POWER SPECTRA

In this Appendix, we compute the power spectra of the mechanical position fluctuations and some of the optical quadratures. In the following, the power spectrum of an operator $\delta\hat{Q}$ is denoted $S_Q[\omega]$, with

$$\begin{aligned} S_Q[\omega] &\equiv \int_{-\infty}^{+\infty} dt e^{i\omega t} \langle \delta\hat{Q}(t) \delta\hat{Q}(0) \rangle \\ &= \int_{-\infty}^{+\infty} \frac{d\omega'}{2\pi} \langle \delta\hat{Q}[\omega] \delta\hat{Q}[\omega'] \rangle, \end{aligned} \quad (\text{C1})$$

and we will also use the notation

$$S_{Q_1 Q_2}[\omega] = \frac{1}{2} \int_{-\infty}^{+\infty} \frac{d\omega'}{2\pi} \langle \delta\hat{Q}_1[\omega] \delta\hat{Q}_2[\omega'] + \delta\hat{Q}_2[\omega] \delta\hat{Q}_1[\omega'] \rangle \quad (\text{C2})$$

for correlators between two operators $\delta\hat{Q}_1$ and $\delta\hat{Q}_2$.

For measurements such as homodyne detection, the relevant spectrum is the symmetrized spectrum $\frac{1}{2}(S_Q[\omega] + S_Q[-\omega])$. Using Eq. (A6), we get

$$S_Q[-\omega] = \sum_{\eta, \eta'} \int_{-\infty}^{+\infty} \frac{d\omega'}{2\pi} c_{\eta}^Q[-\omega] c_{\eta'}^Q[\omega'] \langle \hat{\eta}[-\omega] \hat{\eta}'[\omega'] \rangle, \quad (\text{C3})$$

and, given the noise correlations functions (11) and (12), we have $\langle \hat{\eta}[-\omega] \hat{\eta}'[\omega'] \rangle \propto \delta(\omega' - \omega)$. Therefore, $S_Q[-\omega] = S_Q[\omega]$ and the symmetrized spectrum is also given by Eq. (C1).

1. Mechanical position spectrum

We first compute the mechanical position power spectrum $S_q[\omega]$. Using Eq. (18) and the noise correlation functions (12) and (11), in the frequency domain, we get Eq. (33). In the limit of a purely dispersive optomechanical coupling $g_a^c \rightarrow 0$, we recover Eq. (D10) from [17]. The effective susceptibility, which appears in Eq. (33), is defined by Eq. (20) and the related coefficients $C_{\mu}^{a/d}$ by Eqs. (19). The phonon number in the mechanical fluctuations, Eq. (35), can also be computed

from the position spectrum [41] since

$$\begin{aligned}\langle \delta \hat{q}^2 \rangle &= \int_{-\infty}^{+\infty} \frac{d\omega}{2\pi} S_q[\omega], \\ \langle \delta \hat{p}^2 \rangle &= \int_{-\infty}^{+\infty} \frac{d\omega}{2\pi} \left(\frac{\omega}{\Omega_{\text{mec}}} \right)^2 S_q[\omega].\end{aligned}\quad (\text{C4})$$

Note that, in practice, these integrals only need to be evaluated on a frequency range $[0, \Omega_{\text{max}}]$, with the cutoff frequency Ω_{max} one or two orders of magnitude larger than Ω_{mec} , since the integrands are even functions of ω and $S_q[\omega]$ is sharply peaked at the effective mechanical frequency.

2. Output light spectrum

As a next step, we compute the power spectra, as defined in Eq. (C1), of the quadratures of the light leaking out of the cavity, i.e., $S_{X_{\text{out},\mu}}$ and $S_{P_{\text{out},\mu}}$, where $\hat{X}_{\text{out},\mu} = (\hat{a}_{\text{out},\mu} + \hat{a}_{\text{out},\mu}^\dagger)/\sqrt{2}$ and $\hat{P}_{\text{out},\mu} = (\hat{a}_{\text{out},\mu} - \hat{a}_{\text{out},\mu}^\dagger)/i\sqrt{2}$ are the position and momentum quadratures of the output light. The input-output relation for these quadratures is

$$\begin{aligned}\hat{X}_{\text{out},L} &= \hat{X}_{\text{in},L} - \sqrt{2\tilde{\kappa}_a} \delta \hat{X}_a - \sqrt{2\tilde{\kappa}_d} \delta \hat{X}_d + \sqrt{2c_P} \delta \hat{q}, \\ \hat{P}_{\text{out},L} &= \hat{P}_{\text{in},L} - \sqrt{2\tilde{\kappa}_a} \delta \hat{P}_a - \sqrt{2\tilde{\kappa}_d} \delta \hat{P}_d + \sqrt{2c_X} \delta \hat{q}, \\ \hat{X}_{\text{out},R} &= \hat{X}_{\text{in},R} - \sqrt{2\gamma_a} \delta \hat{X}_a, \\ \hat{P}_{\text{out},R} &= \hat{P}_{\text{in},R} - \sqrt{2\gamma_a} \delta \hat{P}_a\end{aligned}\quad (\text{C5})$$

[see Eq. (17)]. Therefore, we get the output spectra given in Eq. (31). Using the solutions of the Langevin equations, Eq. (A6), and the noise correlation functions, we compute the fluctuation spectra

$$\begin{aligned}S_Q[\omega] &= \frac{1}{2} \sum_{\mu} |c_{X_{\text{in},\mu}}^Q[\omega] - ic_{P_{\text{in},\mu}}^Q[\omega]|^2 \\ &\quad + (2\bar{n}_{\text{mec}} + 1) |c_{\xi}^Q[\omega]|^2, \\ S_{Q_1 Q_2}[\omega] &= \frac{1}{2} \sum_{\mu} [\text{Re}\{ (c_{X_{\text{in},\mu}}^{Q_1}[\omega] - ic_{P_{\text{in},\mu}}^{Q_1}[\omega]) \\ &\quad \times (c_{X_{\text{in},\mu}}^{Q_2}[\omega] - ic_{P_{\text{in},\mu}}^{Q_2}[\omega])^* \}] \\ &\quad + (2\bar{n}_{\text{mec}} + 1) \text{Re}\{ c_{\xi}^{Q_1}[\omega] c_{\xi}^{Q_2}[-\omega] \},\end{aligned}\quad (\text{C6})$$

with $Q, Q_1, Q_2 \in \{X_a, P_a, X_d, P_d, q\}$. The coefficients $c_{\eta}^{P_c}$ are defined in Eqs. (A7) and note that $c_{\eta}^Q[-\omega] = c_{\eta}^Q[\omega]^*$.

In many cases, including all devices considered here, the part of the noise power spectrum coming from the optical environments (vacuum noise) is negligible compared to the thermal noise from the mechanical environment. As a consequence, we have

$$\begin{aligned}S_Q[\omega] &\simeq 2\bar{n}_{\text{mec}} |c_{\xi}^Q[\omega]|^2, \\ S_{Q_1 Q_2}[\omega] &\simeq 2\bar{n}_{\text{mec}} \text{Re}\{ c_{\xi}^{Q_1}[\omega] c_{\xi}^{Q_2}[-\omega] \},\end{aligned}\quad (\text{C7})$$

and, in particular, $S_q[\omega] \simeq 2\Gamma_{\text{mec}} \bar{n}_{\text{mec}} |\chi_{\text{mec}}^{\text{eff}}[\omega]|^2$. The expression for $c_{\xi}^Q[\omega]$ always contains the factor $\sqrt{\Gamma_{\text{mec}} \chi_{\text{mec}}^{\text{eff}}[\omega]}$ [see Eqs. (A7)]. Therefore, $S_{X_{\text{out},L}}[\omega]$ and $S_{P_{\text{out},L}}[\omega]$ can be approximated by $\Gamma_{\text{mec}} |\chi_{\text{mec}}^{\text{eff}}[\omega]|^2$ times a frequency-dependent factor

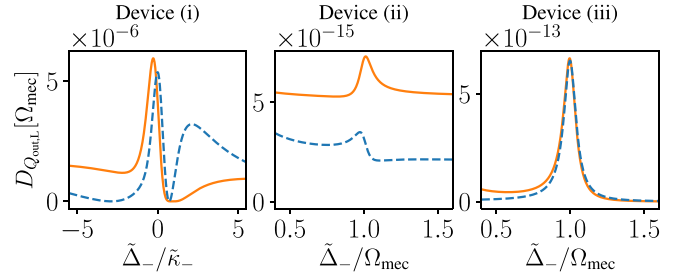


FIG. 12. Factor $D_{Q_{\text{out},L}}[\Omega_{\text{mec}}]$ for $Q = X$ (solid orange) and $Q = P$ (dashed blue) for devices (i)–(iii) as a function of the detuning $\tilde{\Delta}_-$. See Table I for the parameters.

and they hence exhibit a peak at the effective mechanical frequency. However, in all generality, they do not give direct access to $\langle \delta \hat{q}^2 \rangle$ by simple integration over a range of values of ω , $[0, \Omega_{\text{max}}]$, relevant for mechanical features, like in Eq. (C4), because of the frequency-dependent prefactors. We can nonetheless make $S_q[\omega]$ appear in the expression of all the $S_Q[\omega]$ and $S_{Q_1 Q_2}[\omega]$, such that

$$S_{Q_{\text{out},\mu}}[\omega] = S_{Q_{\text{in},\mu}}[\omega] + D_{Q_{\text{out},\mu}}[\omega] S_q[\omega], \quad (\text{C8})$$

with $Q = X, P, \mu = L, R$, and where we have defined

$$\begin{aligned}D_{X_{\text{out},L}}[\omega] &= \left| \sqrt{2c_P} + \sum_c \sqrt{2\tilde{\kappa}_c} (C_q^c[\omega] + C_q^c[-\omega]^*) \right|^2, \\ D_{P_{\text{out},L}}[\omega] &= \left| \sqrt{2c_X} + \sum_c \sqrt{2\tilde{\kappa}_c} i (C_q^c[-\omega]^* - C_q^c[\omega]) \right|^2, \\ D_{X_{\text{out},R}}[\omega] &= 2\gamma_a |C_q^a[\omega] + C_q^a[-\omega]^*|^2, \\ D_{P_{\text{out},R}}[\omega] &= 2\gamma_a |C_q^a[\omega] - C_q^a[-\omega]^*|^2.\end{aligned}\quad (\text{C9})$$

We can then compute $\langle \delta \hat{q}^2 \rangle$ as

$$\langle \delta \hat{q}^2 \rangle = 2 \int_0^{\Omega_{\text{max}}} \frac{d\omega}{2\pi} \frac{S_{Q_{\text{out},\mu}}[\omega] - S_{Q_{\text{in},\mu}}[\omega]}{D_{Q_{\text{out},\mu}}[\omega]}. \quad (\text{C10})$$

Note that for the devices we consider, the frequency dependence of $D_{Q_{\text{out},\mu}}[\omega]$ for $\omega \in [0, \Omega_{\text{max}}]$ is weak, especially for

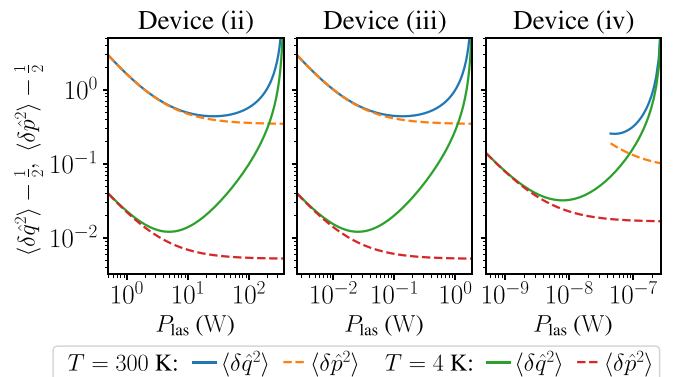


FIG. 13. Mechanical position and momentum fluctuations $\langle \delta \hat{q}^2 \rangle$ and $\langle \delta \hat{p}^2 \rangle$ as a function of laser power for devices (ii), (iii), and (iv). See Tables I and II for the parameters.

device (i), such that $D_{Q_{\text{out},\mu}}[\omega] \simeq D_{Q_{\text{out},\mu}}[\Omega_{\text{mec}}]$ can be taken out of the integral but remains a strongly detuning-dependent prefactor, as evidenced by Fig. 12 and the area plots in Fig. 6.

APPENDIX D: GROUND-STATE COOLING AND ENERGY EQUIPARTITION

In the main text, we showed that devices (ii), (iii), and (iv) can reach $\bar{n}_{\text{fin}} < 1$ (see Figs. 8 and 9). This is, however, not the only requirement to achieve ground-state cooling. The other

condition is that energy equipartition $\langle \delta \hat{q}^2 \rangle \simeq \langle \delta \hat{p}^2 \rangle \simeq \frac{1}{2}$ has to be satisfied. We check this second requirement in Fig. 13 around the laser powers giving $\bar{n}_{\text{fin}} < 1$. We see that energy equipartition eventually breaks down when P_{las} increases, but on a large range of powers before the one giving the minimum phonon number, we have both $\bar{n}_{\text{fin}} < 1$ and $\langle \delta \hat{q}^2 \rangle \simeq \langle \delta \hat{p}^2 \rangle$. This is true both at room temperature (300 K) and at low temperature (4 K), though in the latter case $\langle \delta \hat{q}^2 \rangle$ and $\langle \delta \hat{p}^2 \rangle$ get closer to $\frac{1}{2}$ since the minimum \bar{n}_{fin} is smaller in that case.

-
- [1] M. Aspelmeyer, T. J. Kippenberg, and F. Marquardt, Cavity optomechanics, *Rev. Mod. Phys.* **86**, 1391 (2014).
 - [2] S. Barzanjeh, A. Xuereb, S. Gröblacher, M. Paternostro, C. A. Regal, and E. M. Weig, Optomechanics for quantum technologies, *Nat. Phys.* **18**, 15 (2022).
 - [3] W. Marshall, C. Simon, R. Penrose, and D. Bouwmeester, Towards quantum superpositions of a mirror, *Phys. Rev. Lett.* **91**, 130401 (2003).
 - [4] J. Chan, T. P. M. Alegre, A. H. Safavi-Naeini, J. T. Hill, A. Krause, S. Gröblacher, M. Aspelmeyer, and O. Painter, Laser cooling of a nanomechanical oscillator into its quantum ground state, *Nature (London)* **478**, 89 (2011).
 - [5] J. D. Teufel, T. Donner, D. Li, J. W. Harlow, M. S. Allman, K. Cicak, A. J. Sirois, J. D. Whittaker, K. W. Lehnert, and R. W. Simmonds, Sideband cooling of micromechanical motion to the quantum ground state, *Nature (London)* **475**, 359 (2011).
 - [6] T. A. Palomaki, J. W. Harlow, J. D. Teufel, R. W. Simmonds, and K. W. Lehnert, Coherent state transfer between itinerant microwave fields and a mechanical oscillator, *Nature (London)* **495**, 210 (2013).
 - [7] E. E. Wollman, C. U. Lei, A. J. Weinstein, J. Suh, A. Kronwald, F. Marquardt, A. A. Clerk, and K. C. Schwab, Quantum squeezing of motion in a mechanical resonator, *Science* **349**, 952 (2015).
 - [8] S. Kotler, G. A. Peterson, E. Shojaei, F. Lecocq, K. Cicak, A. Kwiatkowski, S. Geller, S. Glancy, E. Knill, R. W. Simmonds, J. Aumentado, and J. D. Teufel, Direct observation of deterministic macroscopic entanglement, *Science* **372**, 622 (2021).
 - [9] L. Mercier de Lépinay, C. F. Ockeloen-Korppi, M. J. Woolley, and M. A. Sillanpää, Quantum mechanics-free subsystem with mechanical oscillators, *Science* **372**, 625 (2021).
 - [10] S. Gröblacher, J. B. Hertzberg, M. R. Vanner, G. D. Cole, S. Gigan, K. C. Schwab, and M. Aspelmeyer, Demonstration of an ultracold micro-optomechanical oscillator in a cryogenic cavity, *Nat. Phys.* **5**, 485 (2009).
 - [11] E. Verhagen, S. Deléglise, S. Weis, A. Schliesser, and T. J. Kippenberg, Quantum-coherent coupling of a mechanical oscillator to an optical cavity mode, *Nature (London)* **482**, 63 (2012).
 - [12] P. Rabl, Photon blockade effect in optomechanical systems, *Phys. Rev. Lett.* **107**, 063601 (2011).
 - [13] A. Nunnenkamp, K. Børkje, and S. M. Girvin, Single-photon optomechanics, *Phys. Rev. Lett.* **107**, 063602 (2011).
 - [14] J. D. Teufel, D. Li, M. S. Allman, K. Cicak, A. J. Sirois, J. D. Whittaker, and R. W. Simmonds, Circuit cavity electromechanics in the strong-coupling regime, *Nature (London)* **471**, 204 (2011).
 - [15] A. Naesby and A. Dantan, Microcavities with suspended sub-wavelength structured mirrors, *Opt. Express* **26**, 29886 (2018).
 - [16] O. Černotík, A. Dantan, and C. Genes, Cavity quantum electrodynamics with frequency-dependent reflectors, *Phys. Rev. Lett.* **122**, 243601 (2019).
 - [17] J. Monsel, N. Dashti, S. K. Manjeshwar, J. Eriksson, H. Ernbrink, E. Olsson, E. Torneus, W. Wiczorek, and J. Splettstoesser, Optomechanical cooling with coherent and squeezed light: The thermodynamic cost of opening the heat valve, *Phys. Rev. A* **103**, 063519 (2021).
 - [18] J. M. Fitzgerald, S. K. Manjeshwar, W. Wiczorek, and P. Tassin, Cavity optomechanics with photonic bound states in the continuum, *Phys. Rev. Res.* **3**, 013131 (2021).
 - [19] S. Fan, W. Suh, and J. D. Joannopoulos, Temporal coupled-mode theory for the Fano resonance in optical resonators, *J. Opt. Soc. Am. A* **20**, 569 (2003).
 - [20] M. F. Limonov, M. V. Rybin, A. N. Poddubny, and Y. S. Kivshar, Fano resonances in photonics, *Nat. Photon.* **11**, 543 (2017).
 - [21] W. Zhou, D. Zhao, Y.-C. Shuai, H. Yang, S. Chuwongin, A. Chadha, J.-H. Seo, K. X. Wang, V. Liu, Z. Ma, and S. Fan, Progress in 2D photonic crystal Fano resonance photonics, *Prog. Quantum Electron.* **38**, 1 (2014).
 - [22] R. J. Bettles, S. A. Gardiner, and C. S. Adams, Enhanced optical cross section via collective coupling of atomic dipoles in a 2D array, *Phys. Rev. Lett.* **116**, 103602 (2016).
 - [23] E. Shahmoon, D. S. Wild, M. D. Lukin, and S. F. Yelin, Cooperative resonances in light scattering from two-dimensional atomic arrays, *Phys. Rev. Lett.* **118**, 113601 (2017).
 - [24] D. S. Wild, E. Shahmoon, S. F. Yelin, and M. D. Lukin, Quantum nonlinear optics in atomically thin materials, *Phys. Rev. Lett.* **121**, 123606 (2018).
 - [25] S. Kini Manjeshwar, A. Ciers, J. Monsel, H. Pfeifer, C. Peralle, S. M. Wang, P. Tassin, and W. Wiczorek, Integrated micro-cavity optomechanics with a suspended photonic crystal mirror above a distributed Bragg reflector, *Opt. Express* **31**, 30212 (2023).
 - [26] J. M. Dobrindt and T. J. Kippenberg, Theoretical analysis of mechanical displacement measurement using a multiple cavity mode transducer, *Phys. Rev. Lett.* **104**, 033901 (2010).
 - [27] P. Komar, S. D. Bennett, K. Stannigel, S. J. M. Habraken, P. Rabl, P. Zoller, and M. D. Lukin, Single-photon nonlinearities in two-mode optomechanics, *Phys. Rev. A* **87**, 013839 (2013).
 - [28] R. Burgwal and E. Verhagen, Enhanced nonlinear optomechanics in a coupled-mode photonic crystal device, *Nat. Commun.* **14**, 1526 (2023).

- [29] J. D. Thompson, B. M. Zwickl, A. M. Jayich, F. Marquardt, S. M. Girvin, and J. G. E. Harris, Strong dispersive coupling of a high-finesse cavity to a micromechanical membrane, *Nature (London)* **452**, 72 (2008).
- [30] T. K. Paraíso, M. Kalaei, L. Zang, H. Pfeifer, F. Marquardt, and O. Painter, Position-squared coupling in a tunable photonic crystal optomechanical cavity, *Phys. Rev. X* **5**, 041024 (2015).
- [31] I. S. Grudinin, H. Lee, O. Painter, and K. J. Vahala, Phonon laser action in a tunable two-level system, *Phys. Rev. Lett.* **104**, 083901 (2010).
- [32] A. Xuereb, R. Schnabel, and K. Hammerer, Dissipative optomechanics in a michelson-sagnac interferometer, *Phys. Rev. Lett.* **107**, 213604 (2011).
- [33] J. Baraillon, B. Taurel, P. Labeye, and L. Duraffourg, Linear analytical approach to dispersive, external dissipative, and intrinsic dissipative couplings in optomechanical systems, *Phys. Rev. A* **102**, 033509 (2020).
- [34] F. Elste, S. M. Girvin, and A. A. Clerk, Quantum noise interference and backaction cooling in cavity nanomechanics, *Phys. Rev. Lett.* **102**, 207209 (2009).
- [35] C. Peralle, S. K. Manjeshwar, A. Ciers, W. Wiczorek, and P. Tassin, Quasibound states in the continuum in photonic crystal based optomechanical microcavities, *Phys. Rev. B* **109**, 035407 (2024).
- [36] C. W. Gardiner and M. J. Collett, Input and output in damped quantum systems: Quantum stochastic differential equations and the master equation, *Phys. Rev. A* **31**, 3761 (1985).
- [37] W. P. Bowen and G. J. Milburn, *Quantum Optomechanics* (CRC Press, Boca Raton, FL, 2016).
- [38] V. Giovannetti and D. Vitali, Phase-noise measurement in a cavity with a movable mirror undergoing quantum brownian motion, *Phys. Rev. A* **63**, 023812 (2001).
- [39] S. A. Saarinen, S. A. Saarinen, N. Kralj, N. Kralj, N. Kralj, E. C. Langman, E. C. Langman, Y. Tsaturyan, Y. Tsaturyan, A. Schliesser, and A. Schliesser, Laser cooling a membrane-in-the-middle system close to the quantum ground state from room temperature, *Optica* **10**, 364 (2023).
- [40] S. K. Manjeshwar, A. Ciers, F. Hellman, J. Bläsing, A. Strittmatter, and W. Wiczorek, High-Q trampoline resonators from strained crystalline ingap for integrated free-space optomechanics, *Nano Lett.* **23**, 5076 (2023).
- [41] C. Genes, D. Vitali, P. Tombesi, S. Gigan, and M. Aspelmeyer, Ground-state cooling of a micromechanical oscillator: Comparing cold damping and cavity-assisted cooling schemes, *Phys. Rev. A* **77**, 033804 (2008).
- [42] U. DeliĆ, M. Reisenbauer, K. Dare, D. Grass, V. Vuletić, N. Kiesel, and M. Aspelmeyer, Cooling of a levitated nanoparticle to the motional quantum ground state, *Science* **367**, 892 (2020).
- [43] P. Rabl, C. Genes, K. Hammerer, and M. Aspelmeyer, Phase-noise induced limitations on cooling and coherent evolution in optomechanical systems, *Phys. Rev. A* **80**, 063819 (2009).
- [44] T. J. Kippenberg, A. Schliesser, and M. L. Gorodetsky, Phase noise measurement of external cavity diode lasers and implications for optomechanical sideband cooling of GHz mechanical modes, *New J. Phys.* **15**, 015019 (2013).
- [45] X. Zhang, C.-L. Zou, L. Jiang, and H. X. Tang, Cavity magnomechanics, *Sci. Adv.* **2**, e1501286 (2016).
- [46] C. A. Potts, E. Varga, V. A. S. V. Bittencourt, S. V. Kusminskiy, and J. P. Davis, Dynamical backaction magnomechanics, *Phys. Rev. X* **11**, 031053 (2021).
- [47] F. Zou, L. Du, Y. Li, and H. Dong, Amplifying frequency up-converted infrared signals with a molecular optomechanical cavity, *Phys. Rev. Lett.* **132**, 153602 (2024).
- [48] T. E. Li, A. Nitzan, and J. E. Subotnik, Polariton relaxation under vibrational strong coupling: Comparing cavity molecular dynamics simulations against Fermi's golden rule rate, *J. Chem. Phys.* **156**, 134106 (2022).
- [49] B. S. Simpkins, A. D. Dunkelberger, and I. Vurgaftman, Control, modulation, and analytical descriptions of vibrational strong coupling, *Chem. Rev.* **123**, 5020 (2023).
- [50] E. X. DeJesus and C. Kaufman, Routh-Hurwitz criterion in the examination of eigenvalues of a system of nonlinear ordinary differential equations, *Phys. Rev. A* **35**, 5288 (1987).